J. Fluid Mech. (2014), *vol.* 746, *pp.* 368–404. © Cambridge University Press 2014
doi:10.1017/jfm.2014.136

Resonance-driven oscillations in a flexible-channel flow with fixed upstream flux and a long downstream rigid segment

Feng Xu[1], John Billingham[1] and Oliver E. Jensen[2,†]

[1]School of Mathematical Sciences, University of Nottingham, University Park, Nottingham NG7 2RD, UK

[2]School of Mathematics, University of Manchester, Oxford Road, Manchester M13 9PL, UK

(Received 7 August 2013; revised 11 January 2014; accepted 6 March 2014; first published online 3 April 2014)

Flow driven through a planar channel having a finite-length membrane inserted in one wall can be unstable to self-excited oscillations. In a recent study (Xu, Billingham & Jensen *J. Fluid Mech.*, vol. 723, 2013, pp. 706–733), we identified a mechanism of instability arising when the inlet flux and outlet pressure are held constant, and the rigid segment of the channel downstream of the membrane is sufficiently short to have negligible influence on the resulting oscillations. Here we identify an independent mechanism of instability that is intrinsically coupled to flow in the downstream rigid segment, which becomes prominent when the downstream segment is much longer than the membrane. Using a spatially one-dimensional model of the system, we perform a three-parameter unfolding of a degenerate bifurcation point having four zero eigenvalues. Our analysis reveals how instability is promoted by a 1:1 resonant interaction between two modes, with the resulting oscillations described by a fourth-order amplitude equation. This predicts the existence of saturated sawtooth oscillations, which we reproduce in full Navier–Stokes simulations of the same system.

Key words: biological fluid dynamics, channel flow, flow-structure interactions

1. Introduction

In a recent study (Xu, Billingham & Jensen 2013, hereinafter referred to as XBJ), we investigated a mathematical model for flow in a finite-length flexible-walled channel, when the inlet flux and downstream pressure are held fixed. The channel is assumed to contain in one wall a segment of membrane under tension, and is otherwise rigid (figure 1). The problem has its origins in physiology (Knowlton & Starling 1912; Grotberg & Jensen 2004; Heil & Hazel 2011) and applications in microfluidics (Chakraborty *et al.* 2012) but raises some profound fluid-mechanical questions of its own, primarily because of the propensity of the system to undergo self-excited oscillations involving vigorous fluid–structure interaction. Oscillations arise through global instabilities that are strongly coupled to the rigid parts of the system, situated upstream or downstream of the flexible segment. One mechanism of instability onset, operating when the upstream pressure is prescribed, is increasingly

† Email address for correspondence: oliver.jensen@manchester.ac.uk

https://doi.org/10.1017/jfm.2014.136 Published online by Cambridge University Press

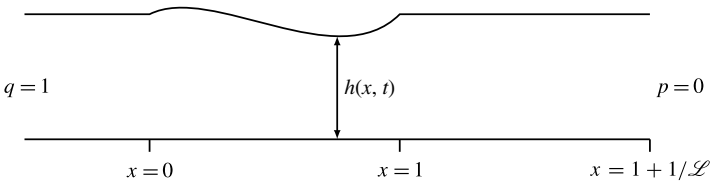


FIGURE 1. The flow domain, showing dimensionless variables and parameters. Flow is from left to right. The membrane occupies $0 < x < 1$; the channel is rigid otherwise.

well understood, having been demonstrated using theoretical models of both a flexible-walled channel (Jensen & Heil 2003; Stewart, Waters & Jensen 2009; Stewart *et al.* 2010) and a finite-length flexible tube (Whittaker *et al.* 2010*a*,*b*,*c*). However this mechanism fails to explain oscillations that have been reported in simulations of a flexible-walled channel when the upstream flux is prescribed (Luo & Pedley 1996, 1998, 2000; Liu, Luo & Cai 2012). In this case, the conditions downstream of the membrane are of particular importance.

If the rigid channel downstream of the membrane is of a length comparable to, or shorter than, the membrane itself, then the pressure drop along this segment is modest, reducing its influence on possible instability mechanisms. In particular, with the upstream flux prescribed, and in a parameter regime near a degenerate bifurcation point, growing oscillations around the uniform state can arise that are driven by divergent instabilities of nearby steady (but unstable) membrane configurations, in a manner that is independent of the downstream segment (XBJ). This instability mechanism is by no means exclusive and its range of applicability is restricted to certain parameter regimes. In order to obtain a broader view of the origin of instabilities, we consider here the case when the downstream rigid segment is substantially longer than the membrane and its role in the dynamics consequently more profound.

A flexible-walled channel supports the propagation of waves, which can reflect from rigid boundaries (Stewart *et al.* 2009). In the parameter regime of interest here, the waves have wavelength comparable to (or longer than) the membrane length, so that membrane disturbances have only one or two extrema. A single-humped oscillation can be expected (by mass conservation) to generate stronger axial sloshing motions in the adjacent rigid segments than a symmetric double-humped oscillation of comparable amplitude. Thus, with pressure conditions prescribed at the inlet and outlet, one-humped oscillations are dominant (Jensen & Heil 2003). In contrast, with the inlet flux prescribed, axial sloshing in the upstream rigid segment is suppressed, and the primary oscillatory instability is to two-humped oscillations (Liu *et al.* 2012). In this case, sloshing motions in the downstream segment can still be important, although there is no longer the potential for membrane oscillations to extract kinetic energy from the mean flow using the mechanism identified by Jensen & Heil (2003).

In developing theoretical models of the system illustrated in figure 1, there is a trade-off between accuracy, complexity and analytic tractability, which is best addressed by gathering understanding from complementary approaches. In the present instance, we choose to investigate a spatially one-dimensional model, supplementing this with two-dimensional simulations. The strengths and weaknesses of the one-dimensional model have been discussed previously (Stewart *et al.* 2009, 2010, XBJ). Briefly, in the absence of a rational closure approximation that is uniformly valid for all Reynolds numbers, the one-dimensional model is necessarily

https://doi.org/10.1017/jfm.2014.136 Published online by Cambridge University Press

qualitative (at best) when viscous effects are weak, making it important to validate predictions using two-dimensional simulations; nevertheless the model predicts a rich variety of behaviour. In contrast, more systematic asymptotic approaches to the flux-driven problem based on interactive boundary-layer theory have so far failed to provide robust evidence for the onset of oscillations (Guneratne & Pedley 2006; Kudenatti, Bujurke & Pedley 2012; Pihler-Puzović & Pedley 2013). Simulations have been used to map out regions of parameter space in which oscillations of different frequencies can arise (Luo & Pedley 1996, 1998, 2000; Liu *et al.* 2012) but insight into fundamental mechanisms from such an approach is necessarily limited.

The physical model we investigate here is defined as follows. The inlet flux is prescribed and the inlet velocity profile is chosen to be that of Poiseuille flow; the outlet pressure is assumed constant. The pressure external to the membrane is then chosen to match that of Poiseuille flow in a uniform channel, ensuring that the flat membrane is a steady configuration. The membrane is assumed to be under sufficiently large tension that changes induced by stretching or by viscous stresses are relatively small. Likewise the membrane is assumed to be sufficiently thin for wall inertia and bending stresses not to be significant. The internal flow is driven at Reynolds numbers that are large enough to induce instability but not so large as to promote transition to turbulence. The uniform state then loses stability in two ways (XBJ): either to non-uniform steady configurations via transcritical bifurcations; or to oscillations via Hopf bifurcations. These states can in turn undergo secondary bifurcations. Instability is typically promoted by increasing the Reynolds number of the flow or reducing the membrane tension.

In XBJ, we focused attention on the primary organising centre in parameter space, namely a point at which a Hopf and transcritical bifurcation arise simultaneously, giving rise to 'mode-2' perturbations (i.e. membrane displacements with two extrema). We were then able to construct amplitude equations describing the evolution of the system in the neighbourhood of this point. The growth of oscillations was shown to be strongly influenced by two nearby saddle points, before switching to large-amplitude 'slamming' motion involving transient near-collapse of the channel. With a short downstream rigid segment, this calculation involved a two-parameter unfolding of a degenerate bifurcation having a double-zero eigenvalue. Here, we investigate the same organising centre but address the more complex case of a longer downstream channel, necessitating a three-parameter unfolding of a degenerate bifurcation with four zero eigenvalues. This additional complexity arises because of a time derivative in a downstream boundary condition, associated with the pressure drop arising from unsteady 'sloshing' motion of the fluid column in the downstream channel. This additional degree of freedom enables the system to sustain additional interacting eigenmodes, with the potential to undergo resonant interactions. This gives us the opportunity to explore an instability mechanism akin to aeroelastic flutter, proposed by Mandre & Mahadevan (2010).

The model is briefly recalled in § 2, and then the linear stability of the uniform state is described in § 3, restricting attention to the neighbourhood of the degenerate bifurcation point. We identify three dominant balances between parameters, associated with three distinct branches of the primary Hopf neutral curve, from which we derive leading-order approximations of the linear stability problem in § 4. One limit, in particular, forms the basis for a weakly nonlinear analysis in § 5, from which we derive a fourth-order amplitude equation. This has two independent parameters and a rich phenomenology, which we sketch briefly. Predictions from this reduced-order model are tested against simulations of the full one-dimensional model and against two-dimensional Navier–Stokes simulations in § 6. Our results are summarised and discussed in § 7.

https://doi.org/10.1017/jfm.2014.136 Published online by Cambridge University Press

2. Formulation

We consider a rigid planar channel of width a for which part of one wall is replaced by a massless membrane of undeformed length L^*, elastic modulus E and thickness h_0^* under initial longitudinal tension T_0. Fluid of dynamic viscosity μ and density ρ is driven through the channel with a given Poiseuille flow profile at the inlet and zero pressure at the outlet (figure 1). The lengths of the rigid upstream and downstream segments of the channel are L_1^* and L_2^*, respectively. We impose a linear distribution of external pressure on the membrane such that the undeformed configuration admits steady Poiseuille flow along the whole channel.

We introduce Cartesian coordinates (x^*, y^*) so that the channel walls lie at $y^* = 0$ and $y^* = a$ (where the channel walls are rigid, that is for $-L_1^* \leqslant x^* < 0$ and $L^* < x^* \leqslant L^* + L_2^*$), or $y^* = 0$ and $y^* = h^*(x^*, t^*)$ (where the channel wall is flexible, for $0 \leqslant x^* \leqslant L^*$). Here $h^*(0, t^*) = h^*(L^*, t^*) = a$ for all time t^*. The flow field is $(u^*(x^*, y^*, t^*), v^*(x^*, y^*, t^*))$. We denote the axial flux by $q^*(x^*, t^*) = \int_0^{h^*} u^* \mathrm{d}y^*$. Given a fixed upstream flux $q_0 = q^*(-L_1^*, t^*)$, we introduce a velocity scale $U_0 = q_0/a$. After non-dimensionlising by the velocity scale U_0, the length scale a, the time scale a/U_0 and the pressure scale ρU_0^2, we obtain the dimensionless Navier–Stokes equations governing the flow in the channel, as given for example in Jensen & Heil (2003). Supplementing the Navier–Stokes equations with the large-displacement Kirchhoff–Love beam equation governing the deformation of the membrane, we obtain a two-dimensional fully coupled fluid–structure interaction problem (Jensen & Heil 2003), which we solve numerically using a demonstration-driver from the finite-element library oomph-lib (Heil & Hazel 2006).

The two-dimensional problem is characterised by seven dimensionless parameters

$$\left.\begin{aligned} L_1 &= \frac{L_1^*}{a}, \quad L = \frac{L^*}{a}, \quad L_2 = \frac{L_2^*}{a}, \quad h_0 = \frac{h_0^*}{a}, \\ \mathscr{Q} &= \frac{\mu U_0}{Ea}, \quad \mathscr{R} = \frac{\mu L^*}{\rho a^2 U_0}, \quad T = \frac{T_0 a}{\rho U_0^2 L^{*2}}. \end{aligned}\right\} \tag{2.1}$$

The parameter $\mathscr{Q}$ indicates the strength of the fluid–structure interaction, $\mathscr{R}$ measures the strength of viscous effects (a form of inverse Reynolds number) and T is a dimensionless tension. Under small viscous stress ($L/\mathscr{R} \gg 1$), the variation of the initial longitudinal tension along the membrane is negligible (Pedley 1992). From (2.3) in Jensen & Heil (2003) we infer that during flow-induced wall deformation, changes in membrane tension due to stretching are small compared to T if $L^5 \mathscr{Q} T/(\mathscr{R} h_0) \gg 1$ and the effects of bending are small if $L^5 \mathscr{Q} T/(\mathscr{R} h_0^3) \gg 1$. In two-dimensional simulations we subject the ends of the beam to pinned boundary conditions, fixing their positions but allowing them to rotate freely; we set the wall thickness $h_0 = 0.01$ and $\mathscr{Q} = 0.01$, and choose appropriate values of other parameters to ensure the viscous stress, wall stretching and the wall bending terms are all negligibly small. (For a detailed discussion of these effects see Cai & Luo 2003.) Simulations are reported in § 6 below.

By employing a long-wavelength assumption ($L \gg 1$), assuming a self-similar velocity profile (here we choose the Poiseuille profile $u = 6qy(h - y)/h^3$) (see XBJ; Stewart *et al.* 2009, 2010) and neglecting wall stretching, wall bending and viscous

https://doi.org/10.1017/jfm.2014.136 Published online by Cambridge University Press

stresses on the wall, the two-dimensional system can be reduced to the one-dimensional system

$$h_t + q_x = 0, \tag{2.2a}$$

$$q_t + \frac{6}{5}\left(\frac{q^2}{h}\right)_x = Thh_{xxx} + 12\mathscr{R}\left(h - \frac{q}{h^2}\right), \tag{2.2b}$$

for $0 \leqslant x \leqslant 1$. Here $x = x^*/L^*$, $y = y^*/a^*$, $t = t^*U_0/L^*$. The variables $h(x, t) = h^*/a$ and $q(x, t) = q^*/q_0$ are the dimensionless membrane location and axial volume flux, which are subject to the boundary conditions

$$h = 1 \quad (x = 0), \tag{2.3a}$$

$$q = 1 \quad (x = 0), \tag{2.3b}$$

$$h = 1 \quad (x = 1), \tag{2.3c}$$

$$\mathscr{L}Th_{xx} = -(12\mathscr{R}(q-1) + q_t) \quad (x = 1), \tag{2.3d}$$

where $\mathscr{L} = L/L_2$. In (2.2*b*), the pressure gradient within the channel has a contribution from membrane curvature (Th_{xxx}) and a contribution from the linear external pressure gradient ($12\mathscr{R}$). Equation (2.3*d*) accounts for viscous and unsteady pressure drops along the downstream rigid segment in $1 < x < 1 + 1/\mathscr{L}$. Here we focus our attention on the case where the downstream rigid segment is longer than the membrane, that is $\mathscr{L} \ll 1$. We first examine the linear stability of the uniform state $h = 1$, $q = 1$.

3. Linear stability of the uniform state

Setting

$$h = 1 + \mathrm{Re}(H(x)\mathrm{e}^{\sigma t}), \quad q = 1 + \mathrm{Re}(Q(x)\mathrm{e}^{\sigma t}), \tag{3.1a,b}$$

where H, Q and σ are complex, $|H(x)| \ll 1$, $|Q(x)| \ll 1$ and $\mathrm{Re}(\sigma)$ is a growth rate, we obtain from (2.2) and (2.3) the linear eigenvalue problem

$$Q' = -\sigma H, \tag{3.2a}$$

$$TH''' + \tfrac{6}{5}H' + 36\mathscr{R}H - \tfrac{12}{5}Q' - 12\mathscr{R}Q = \sigma Q, \tag{3.2b}$$

with boundary conditions

$$H(0) = 0, \quad Q(0) = 0, \tag{3.3a}$$

$$H(1) = 0, \quad \mathscr{L}TH''(1) + 12\mathscr{R}Q(1) = -\sigma Q(1). \tag{3.3b}$$

We use a Chebyshev approximation to solve (3.2) and (3.3), using the method given in XBJ. We denote eigenmodes as 'mode n' when $|H(x)|$ has n humps.

As explained in XBJ, when $\mathscr{R} = 0$, the linearised equations (3.2) and (3.3) admit simple solutions for which $\sigma = 0$, $Q(x) = 0$, $H = \sin n\pi x$ and $T = T_{n0} = 6/(5n^2\pi^2)$ ($n = 1, 2, 3, \ldots$). These stationary eigenmodes are a manifestation of the Bernoulli effect: membrane curvature induces a non-uniform pressure in the channel, which is accommodated by convective acceleration as the flow slows and quickens where the channel widens and narrows. In the $(T, \mathscr{R})$-plane for fixed $\mathscr{L}$, neutral curves $\sigma = 0$ connect $(T_{10}, 0)$ to $(T_{20}, 0)$ and $(T_{30}, 0)$ to $(T_{40}, 0)$, while a neutral curve $\mathrm{Re}(\sigma) = 0$ emerges from $(T_{20}, 0)$. In the following, we focus on the neutral curves in the vicinity of the degenerate bifurcation point $(T, \mathscr{R}) = (T_{20}, 0)$. This is an interesting point to consider because (3.2) and (3.3) with $\mathscr{R} = 0$ also admit the steady single-humped solution $Q = 0$, $H = 1 - \cos 2\pi x$ provided $\mathscr{L} \to 0$ in (3.3*b*). For $0 < \mathscr{L} \ll 1$, we anticipate that this mode can coexist with the double-humped $H = \sin 2\pi x$ mode if both vary slowly with time, provided slow axial sloshing $Q(1)$ is sufficient to balance the non-zero pressure $H''(1)$ of the single-humped mode.

https://doi.org/10.1017/jfm.2014.136 Published online by Cambridge University Press

3.1. *Numerical results*

The linearised equations (3.2) and (3.3) show that static neutral curves (on which $\sigma = 0$) are independent of $\mathscr{L}$ while oscillatory neutral curves (on which $\sigma \neq 0$) depend on $\mathscr{L}$. This is illustrated by figure 2(*a*), which shows static and oscillatory neutral curves in $(T, \mathscr{R})$-parameter space for $\mathscr{L} = 1$, 0.1 and 0.01 (a wider view of $(T, \mathscr{R})$-parameter space is given in XBJ). The static neutral curve in $T > T_{20}$, labelled TC_2, defines a transcritical bifurcation to a mode-2 steady solution; the oscillatory neutral curve in $T < T_{20}$, labelled Hopf_2, defines a Hopf bifurcation to mode-2 oscillations. The uniform state is linearly stable for $\mathscr{R}$ values above each neutral curve. As $\mathscr{L}$ decreases, a wobble appears on the Hopf_2 curve and the parameter range over which the uniform state is stable reduces. Defining $\mathscr{T} = T - T_{20}$, figure 2(*b*) shows in greater detail some mode-2 oscillatory neutral curves in $(-\mathscr{T}, \mathscr{R})$-space (together with their asymptotic approximations, derived below). As $\mathscr{L}$ decreases, the wobble in the Hopf_2 curve becomes more evident and it lies closer to $T = T_{20}$; we can then identify distinct upper-, lower- and middle-branch behaviour. As $\mathscr{R}$ decreases for fixed $\mathscr{L}$, first $-\mathscr{T}$ decreases like $O(\mathscr{R}^2)$ on the upper branch, then $-\mathscr{T}$ increases on the middle branch, and finally $-\mathscr{T}$ decreases like $O(\mathscr{R})$ on the lower branch. Figure 2(*c*) demonstrates the corresponding frequency of neutrally stable eigenmodes on the Hopf_2 curve. On the upper branch, the frequency of mode-2 oscillations is approximately $\sqrt{27\mathscr{L}/8}$ (as we show in (4.12) below), independent of $-\mathscr{T}$. However, the frequency is approximately $4\pi^2\sqrt{-\mathscr{T}/15}$ (see (4.26) below) on the lower branch, independent of $\mathscr{L}$. This suggests that upper-branch oscillations, for which the dimensional frequency scales like $U_0/\sqrt{L^* L_2^*}$, must induce a sloshing motion in the downstream rigid segment. (The scaling of frequency with $\sqrt{L}$ can be understood by assuming $H = O(1)$ in (3.2) and (3.3) with $|\sigma| \ll 1$, so that $Q = O(|\sigma|)$ from (3.2*a*); balancing the first and last terms in the pressure boundary condition in (3.3*b*), with $T \approx T_{20}$, yields $\mathscr{L} = O(|\sigma|^2)$. Meanwhile the membrane shape is given to leading order by the quasi-static balance $T_{20}H''' + (6/5)H' = 0$ in (3.2*b*).)

Figure 3 depicts eigenvalue paths as the parameter pair $(-\mathscr{T}, \mathscr{R})$ crosses the Hopf_2 curve close to the turning point between the middle and lower branches. As seen in figure 3(*a*), for $\mathscr{R} = 6 \times 10^{-4}$ and $-\mathscr{T} = 10^{-6}$, there exist two pairs of complex-conjugate eigenvalues with almost the same negative real part, both of which are mode 2. As $-\mathscr{T}$ increases, the imaginary part of the conjugate pair with large imaginary part falls while that of the conjugate pair with small imaginary part rises, until they nearly coalesce. Then, the real part of the higher-frequency modes ascends through zero, which corresponds to crossing the middle branch of the neutral curve in figure 2(*b*). Subsequently, the pair collide and split into two positive real eigenvalues. In the meantime, the lower-frequency pair remain stable but coalesce and become two negative real eigenvalues. The eigenvalue path in figure 3(*c*), for $\mathscr{R} = 2 \times 10^{-4}$, is similar to that in figure 3(*a*) except that it is the lower-frequency modes that become unstable on crossing the lower branch of the neutral curve; this resembles the behaviour analysed in XBJ. The intermediate case is shown in figure 3(*b*). This mode interaction is strongly reminiscent of a 1:1 resonance, and suggests a possible mechanism of self-excited oscillation consistent with the conjecture of Mandre & Mahadevan (2010). Figure 2(*c*) shows how the frequency of neutral modes approaches zero as $\mathscr{L} \to 0$, $\mathscr{T} \to 0$ and $\mathscr{R} \to 0$. Thus the structure illustrated in figure 3 collapses to the origin in this limit, yielding four zero eigenvalues.

For larger $\mathscr{R}$, corresponding to moving up the middle and upper branches of the Hopf_2 curve, there are further changes to the pattern of eigenvalues. Figure 4

https://doi.org/10.1017/jfm.2014.136 Published online by Cambridge University Press

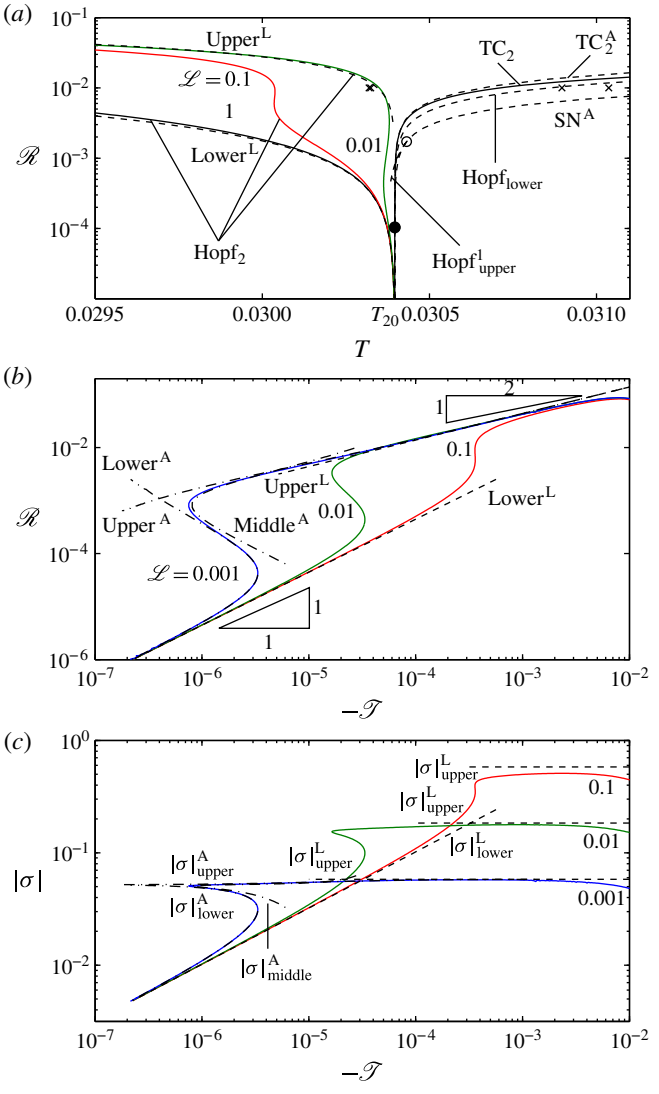


FIGURE 2. (Colour online) (*a*) Neutral curves of static mode-2 perturbations (in $T > T_{20}$, labelled TC_2, solid) and of oscillatory mode-2 perturbations (in $T < T_{20}$, labelled Hopf_2, solid) for $\mathscr{L} = 1$, 0.1 and 0.01. Dashed lines show the asymptotes (4.11) (labelled $\mathrm{Upper}^{\mathrm{L}}$) and (4.25) (labelled $\mathrm{Lower}^{\mathrm{L}}$), the asymptotes (5.14) and (5.15) (labelled $\mathrm{TC}_2^{\mathrm{A}}$ and SN^{A}) and the asymptotes (B 3) for $\mathscr{L} = 0.01$ (labelled $\mathrm{Hopf}_{\mathrm{lower}}$) that coalesces with the SN^{A} at the closed circle. The open circle on SN^{A} denotes a Takens–Bogdanov point. The crosses denote the parameters used in the PDE simulations in § 6. (*b*) Hopf_2 curves for $\mathscr{L} = 0.1$, 0.01 and 0.001 (solid), in addition to the dashed lines showing the asymptotes (4.11) (labelled $\mathrm{Upper}^{\mathrm{L}}$) and (4.25) (labelled $\mathrm{Lower}^{\mathrm{L}}$) and dash-dot lines showing the asymptotes (4.9) (labelled $\mathrm{Upper}^{\mathrm{A}}$), (4.19) and (4.20) (labelled $\mathrm{Lower}^{\mathrm{A}}$) and (4.31) and (4.32) (labelled $\mathrm{Middle}^{\mathrm{A}}$) for $\mathscr{L} = 0.001$. (*c*) Frequency of neutral mode-2 oscillations for $\mathscr{L} = 0.1$, 0.01 and 0.001 (solid), as well as dashed lines showing the asymptotes (4.12) (labelled $|\sigma|^{\mathrm{L}}_{\mathrm{upper}}$) and (4.26) (labelled $|\sigma|^{\mathrm{L}}_{\mathrm{lower}}$); the dash-dot lines show the asymptotes (4.10) (labelled $|\sigma|^{\mathrm{A}}_{\mathrm{upper}}$), (4.19) and (4.20) (labelled $|\sigma|^{\mathrm{A}}_{\mathrm{lower}}$) and (4.31) and (4.32) (labelled $|\sigma|^{\mathrm{A}}_{\mathit{middle}}$) for $\mathscr{L} = 0.001$.

https://doi.org/10.1017/jfm.2014.136 Published online by Cambridge University Press

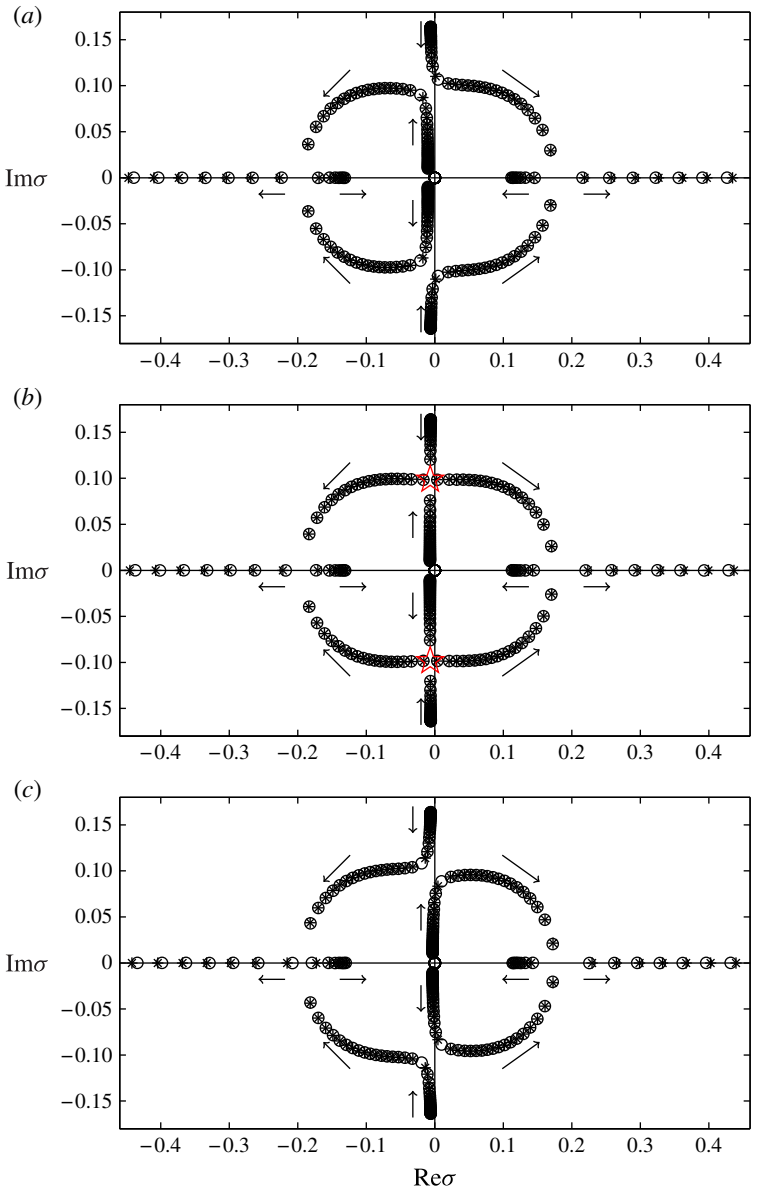


FIGURE 3. (Colour online) Eigenvalue paths as $-\mathscr{T}$ varies from 10^{-6} to 10^{-3} with $\mathscr{L} = 0.01$ and (*a*) $\mathscr{R} = 6 \times 10^{-4}$, (*b*) $\mathscr{R} = 4.27 \times 10^{-4}$ (from (4.21)) and (*c*) $\mathscr{R} = 2 \times 10^{-4}$. Circles represent numerical results from (3.2) and (3.3) while asterisks represent asymptotic results from (4.19) and (4.20) for the same value of $\mathscr{T}$. In (*b*), the two stars are the pair of eigenvalues on coalescence, from (4.23). Arrows show increasing $-\mathscr{T}$.

illustrates the eigenvalue paths towards the upper end of the upper branch. As $-\mathscr{T}$ increases, the eigenvalue pair with initially higher frequency remains stable, while two real eigenvalues coalesce to form a conjugate pair that become unstable.

In figure 5 we replot the oscillatory neutral curves of figure 2(*b*) to reveal their dependence on $\mathscr{L}$. In figure 5(*a*) we plot $-\mathscr{T}/\mathscr{L}$ versus $\mathscr{R}/\mathscr{L}^{1/2}$ and find that the

https://doi.org/10.1017/jfm.2014.136 Published online by Cambridge University Press

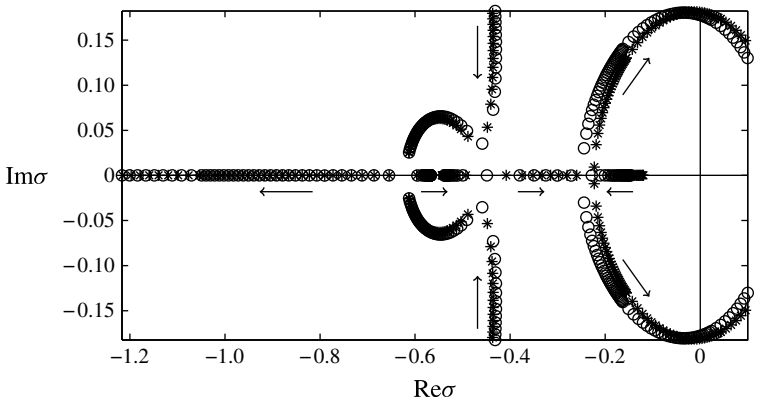


FIGURE 4. Eigenvalue path as T varies from 0.0306 to 0.028 with $\mathscr{L} = 0.01$ and $\mathscr{R} = 1/22$. Circles represent numerical results from (3.2) and (3.3) while asterisks represent asymptotic results from (4.8).

upper branches of the neutral curves coalesce, which suggests that the upper branch has the scaling $\mathscr{R}^2 \sim -\mathscr{T} \sim \mathscr{L}$ as $\mathscr{L} \to 0$, $\mathscr{T} \to 0$ and $\mathscr{R} \to 0$, with an asymptote $1 \gg \mathscr{R}^2 \sim -\mathscr{T} \gg \mathscr{L}$ at its upper end. (We recall from XBJ that TC_2 also follows the scaling $\mathscr{T} \sim \mathscr{R}^2$, independent of $\mathscr{L}$.) Similarly, by plotting $-\mathscr{T}/\mathscr{L}$ versus $\mathscr{R}/\mathscr{L}$, collapse of the data in figure 5(*c*) suggests the lower turning point has the scaling $\mathscr{R} \sim -\mathscr{T} \sim \mathscr{L}$, with $\mathscr{R} \sim -\mathscr{T} \ll \mathscr{L}$ along the lower end of the lower branch. For the middle branch, we plot $-\mathscr{T}/\mathscr{L}^{3/2}$ versus $\mathscr{R}/\mathscr{L}^{1/2}$ (figure 5*b*). In this case, a rough coalescence can be seen, sufficient to motivate investigation of this scaling relationship. Equivalently, the Reynolds number based on channel width, $Re = \rho q_0/\mu$, satisfies $1 \ll Re \ll \sqrt{L_2^* L^*}/a$ on the upper limit of the upper branch of the Hopf curve and $Re \gg L_2/a$ on the lower extremity of the lower branch.

4. Parametric asymptotics

We now seek asymptotic approximations of the linear stability problem by expanding the solution in the neighbourhood of $(\mathscr{T}, \mathscr{R}, \mathscr{L}) = (0, 0, 0)$, seeking to unfold the patterns traced out by the four eigenvalues close to the origin. We assume different relations between the parameters in order to capture behaviour on the lower, middle and upper branches of the $Hopf_2$ curve. We make expansions using

$$Q(x) = Q_0(x) + \epsilon Q_1(x) + \epsilon^2 Q_2(x) + \epsilon^3 Q_3(x) + \cdots, \tag{4.1a}$$

$$H(x) = H_0(x) + \epsilon H_1(x) + \epsilon^2 H_2(x) + \epsilon^3 H_3(x) + \cdots, \tag{4.1b}$$

$$\sigma = \epsilon\sigma_1 + \epsilon^2\sigma_2 + \epsilon^3\sigma_3 + \cdots, \tag{4.1c}$$

where $0 < \epsilon \ll 1$ is a tuning parameter; the coefficients in (4.1) are assumed to be of order unity as $\epsilon \to 0$. Details of the expansions are provided in appendix A.

4.1. *Upper branch:* $\mathscr{R}^2 \sim -\mathscr{T} \sim \mathscr{L}$

Motivated by figure 5(*a*) we scale the parameters as

$$\mathscr{T} = \epsilon^2 \mathscr{T}_2, \quad \mathscr{R} = \epsilon \mathscr{R}_1, \quad \mathscr{L} = \epsilon^2 \mathscr{L}_2. \tag{4.2a,b,c}$$

Here $\mathscr{T}_2$, $\mathscr{R}_1$ and $\mathscr{L}_2$ are assumed to be of order unity as $\epsilon \to 0$. Upon substituting (4.1) and (4.2) into (3.2) and (3.3), one homogeneous system (A 1) and a series of

https://doi.org/10.1017/jfm.2014.136 Published online by Cambridge University Press

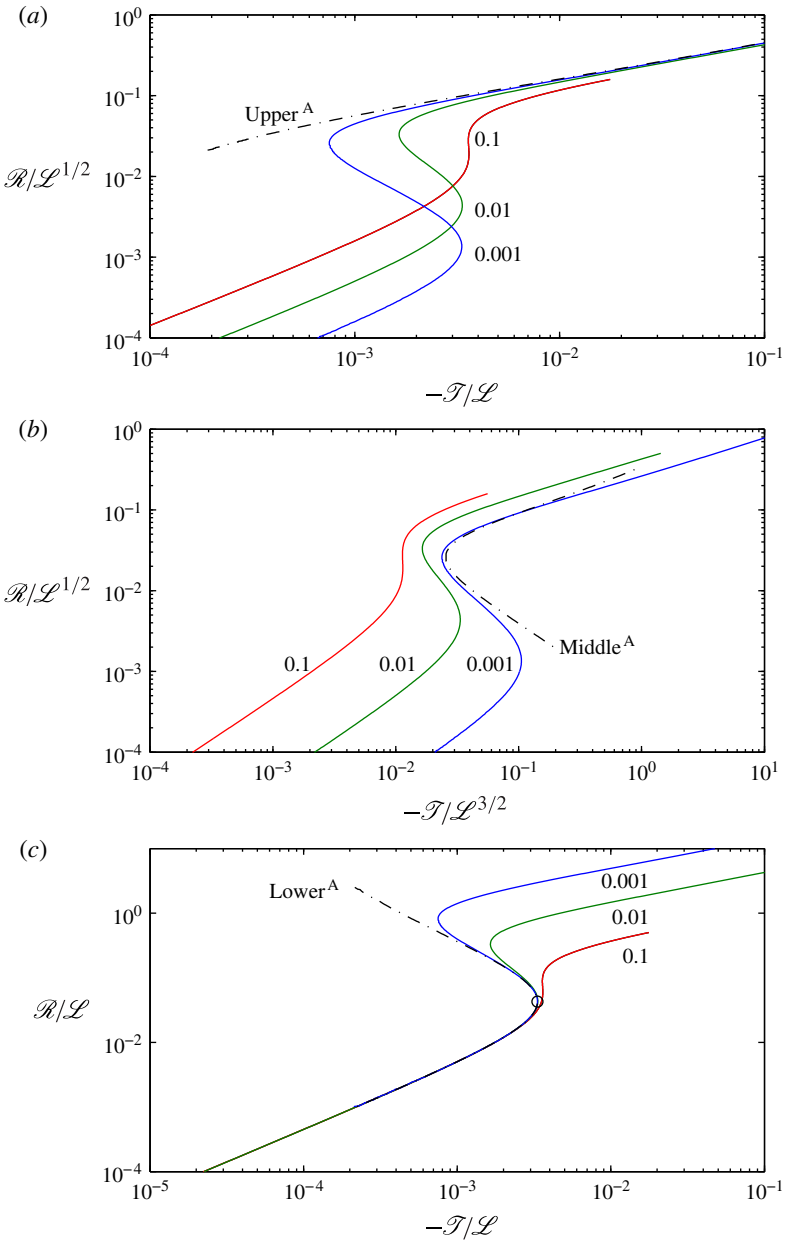


FIGURE 5. (Colour online) Oscillatory mode-2 neutral curves for $\mathscr{L}=0.1$, 0.01 and 0.001 (solid), in addition to the dash-dot lines showing the asymptotes (4.9) (labelled Upper^{A}), (4.19) and (4.20) (labelled Lower^{A}) and (4.31) and (4.32) (labelled Middle^{A}). The circle in (*c*) represents the coalescence point from (4.21) and (4.22).

inhomogeneous systems (A 2) and (A 3) are recovered in succession. Solutions of (A 1) can be derived directly. For each inhomogeneous system, the existence of non-trivial solutions requires a solvability condition, which provides conditions on coefficients appearing at previous orders.

https://doi.org/10.1017/jfm.2014.136 Published online by Cambridge University Press

At $O(1)$, solutions of (A 1) are

$$Q_0 = 0, \quad H_0 = A_0 \sin 2\pi x + B_0(1 - \cos 2\pi x). \tag{4.3a,b}$$

Here A_0 and B_0 are constants. The A_0 component is a typical 'mode-2' solution, whereas the B_0 component has the same wavelength but a single extremum in h at the mid-point of the membrane.

At $O(\epsilon)$, the solvability condition of (A 5) requires $B_0 = 0$, which admits solutions

$$Q_1 = A_0\sigma_1(\cos 2\pi x - 1)/2\pi, \tag{4.4a}$$
$$H_1 = A_1 \sin 2\pi x + B_1(1 - \cos 2\pi x) + A_0(15\mathscr{R}_1 + \sigma_1)x \sin 2\pi x. \tag{4.4b}$$

Here A_1 and B_1 are constants. Thus the single-humped mode (B_1) persists but with smaller magnitude than the primary mode-2 component. The flux Q_1 describes to-and-fro sloshing beneath the membrane generated by the A_0 mode; note that $Q_1(1) = 0$, so that no sloshing is induced in the downstream rigid channel segment at this order. However, weak pressure fluctuations in this segment are apparent, proportional to

$$H_{1xx}(1) = 4\pi A_0(15\mathscr{R}_1 + \sigma_1) + 4\pi^2 B_1. \tag{4.5}$$

These are associated with small asymmetries in membrane shape about its mid-point due to viscous and unsteady effects, and membrane curvature arising via the single-humped B_1 mode. These fluctuations drive downstream axial sloshing at the next order.

At $O(\epsilon^2)$, the solvability conditions of (A 3) give the conditions

$$B_1 = -\frac{A_0(15\mathscr{R}_1 + \sigma_1)(12\mathscr{L}_2 + 5\sigma_1(12\mathscr{R}_1 + \sigma_1))}{4\pi^2(6\mathscr{L}_2 - 5\sigma_1(12\mathscr{R}_1 + \sigma_1))}, \tag{4.6a}$$

$$\mathscr{T}_2 = \frac{3\left(6\mathscr{L}_2\left(1350\mathscr{R}_1^2 + 168\mathscr{R}_1\sigma_1 + 5\sigma_1^2\right) + \sigma_1(12\mathscr{R}_1 + \sigma_1)\left(1350\mathscr{R}_1^2 + 240\mathscr{R}_1\sigma_1 + 11\sigma_1^2\right)\right)}{16\pi^4(6\mathscr{L}_2 - 5\sigma_1(12\mathscr{R}_1 + \sigma_1))}, \tag{4.6b}$$

which admit solutions H_2 and Q_2. We find that

$$Q_2(1) = \sigma_1\left(\frac{15\mathscr{R}_1 + \sigma_1}{2\pi}A_0 - B_1\right) = -\frac{18\mathscr{L}_2 B_1}{12\mathscr{L}_2 + 5\sigma_1(12\mathscr{R}_1 + \sigma_1)}, \tag{4.7}$$

which is a weak axial flux driven by the single-humped (B_1) mode and asymmetries of the double-humped (A_0) mode, with coupling mediated by the downstream rigid channel length via $\mathscr{L}$. The first condition (4.6*a*) slaves the single-humped mode to the primary mode-2 solution. The second condition (4.6*b*) gives a quartic for σ_1, which we re-express as

$$\begin{aligned} &12\mathscr{L}\left(2025\mathscr{R}^2 - 8\pi^4\mathscr{T}\right) + 24\mathscr{R}\left(2025\mathscr{R}^2 + 126\mathscr{L} + 40\pi^4\mathscr{T}\right)\sigma \\ &\quad + 10\left(1269\mathscr{R}^2 + 9\mathscr{L} + 8\pi^4\mathscr{T}\right)\sigma^2 + 1116\mathscr{R}\sigma^3 + 33\sigma^4 = 0. \end{aligned} \tag{4.8}$$

Figure 4 shows how (4.8) successfully approximates the solution of (3.2) and (3.3).

https://doi.org/10.1017/jfm.2014.136 Published online by Cambridge University Press

If we assume σ is purely imaginary and isolate the real and imaginary parts of (4.8), we obtain explicit expressions for the upper branch of the Hopf_2 curve and the corresponding neutral frequency as

$$\mathscr{T} = \frac{9\left(-1183\mathscr{L} - 59700\mathscr{R}^2 + 31\sqrt{3}\sqrt{\left(3\mathscr{L} + 200\mathscr{R}^2\right)\left(161\mathscr{L} + 2400\mathscr{R}^2\right)}\right)}{4000\pi^4}, \tag{4.9}$$

and

$$\sigma = \pm\mathrm{i}\sqrt{\frac{21\mathscr{L}}{50} - 72\mathscr{R}^2 + \frac{3}{50}\sqrt{3}\sqrt{483\mathscr{L}^2 + 39\,400\mathscr{L}\mathscr{R}^2 + 480\,000\mathscr{R}^4}}. \tag{4.10}$$

Good agreement between (4.9) and (4.10) and predictions from the linearised equations (3.2) and (3.3) can be seen in figure 2(*b*,*c*) and figure 5(*a*), although the approximation (4.9) (labelled $\mathrm{Upper}^{\mathrm{A}}$ in figure 2(*b*)) does not capture the upper turning point in the neutral curve.

Assuming $1 \gg \mathscr{R}^2 \sim -\mathscr{T} \gg \mathscr{L}$ in (4.9), the upper branch of the Hopf_2 curve asymptotes to

$$-\mathscr{T} = \frac{405}{8\pi^4}\mathscr{R}^2, \tag{4.11}$$

shown in figure 2(*a*,*b*) as $\mathrm{Upper}^{\mathrm{L}}$; the approximate neutral frequency in (4.10) becomes

$$\sigma = \pm\mathrm{i}\sqrt{\frac{27\mathscr{L}}{8}}, \tag{4.12}$$

as shown in figure 2(*c*). Interestingly, the neutral curve asymptote (4.11) is independent of $\mathscr{L}$, whereas the oscillation frequency (4.12) is independent of $\mathscr{T}$. In addition, setting $\sigma = 0$ in (4.8) recovers the locations of the TC_2 curve, $\mathscr{T} = 2025\mathscr{R}^2/8\pi^4$ provided $\mathscr{L} > 0$ (XBJ), shown as $\mathrm{TC}_2^{\mathrm{A}}$ in figure 2(*a*).

Assuming $\mathscr{L}^{3/2} \ll \mathscr{T} \ll \mathscr{L} \sim \mathscr{R}^2$, by balancing terms in (4.8) at increasing order, we derive eigenvalues

$$\sigma = \overline{\sigma_1} + \overline{\sigma_2} + \cdots, \tag{4.13}$$

where $\overline{\sigma_1} \gg \overline{\sigma_2}$ and $\overline{\sigma_1}, \overline{\sigma_2}$ satisfy

$$8100\mathscr{L}\mathscr{R}^2 + 72\mathscr{R}\left(14\mathscr{L} + 225\mathscr{R}^2\right)\overline{\sigma_1} + 30\left(\mathscr{L} + 141\mathscr{R}^2\right)\overline{\sigma_1}^2 + 372\mathscr{R}\overline{\sigma_1}^3 + 11\overline{\sigma_1}^4 = 0, \tag{4.14a}$$

$$\overline{\sigma_2} = -\left[96\pi^4\mathscr{T}\,\overline{\sigma_1}(12\mathscr{R} + \overline{\sigma_1})(15\mathscr{R} + \overline{\sigma_1})^2\right] \Big/ \left[2^3 3^7 5^4\mathscr{R}^5 + 2^2 3^5 5^3 47\mathscr{R}^4\overline{\sigma_1} + 2^3 3^3 5 \times 23 \times 43\mathscr{R}^3\overline{\sigma_1}^2 + 2^2 3^2 13 \times 197\mathscr{R}^2\overline{\sigma_1}^3 + 3702\mathscr{R}\overline{\sigma_1}^4 + 55\overline{\sigma_1}^5\right], \tag{4.14b}$$

respectively, which represent the overlap with the middle branch, as we will see below.

4.2. *Lower branch:* $\mathscr{R} \sim -\mathscr{T} \sim \mathscr{L}$

Motivated by figure 5(*c*) we now assume

$$\mathscr{T} = \epsilon^2\mathscr{T}_2, \quad \mathscr{R} = \epsilon^2\mathscr{R}_2, \quad \mathscr{L} = \epsilon^2\mathscr{L}_2. \tag{4.15a,b,c}$$

Here $\mathscr{T}_2$, $\mathscr{R}_2$ and $\mathscr{L}_2$ are assumed to be of order unity as $\epsilon \to 0$. Upon substituting (4.1) and (4.15) into the linearised equations (3.2) and (3.3), one homogeneous

https://doi.org/10.1017/jfm.2014.136 Published online by Cambridge University Press

system and a series of inhomogeneous systems (see Appendix A.2) are recovered in succession, following the pattern in the upper-branch calculation.

At $O(1)$, solutions of (A 4) are as in (4.3). At $O(\epsilon)$, the solvability condition of (A 2) is again $B_0 = 0$, which admits solutions

$$Q_1 = A_0\sigma_1(\cos 2\pi x - 1)/2\pi, \tag{4.16a}$$

$$H_1 = A_1 \sin 2\pi x + B_1(1 - \cos 2\pi x) + A_0\sigma_1 x \sin 2\pi x, \tag{4.16b}$$

missing a viscous term present in (4.4*b*).

At $O(\epsilon^2)$, the solvability conditions of (A 6) are

$$B_1 = -\frac{A_0\sigma_1\left(12\mathscr{L}_2 + 5\sigma_1^2\right)}{4\pi^2\left(6\mathscr{L}_2 - 5\sigma_1^2\right)}, \quad \mathscr{T}_2 = \frac{3\sigma_1^2\left(30\mathscr{L}_2 + 11\sigma_1^2\right)}{16\pi^4\left(6\mathscr{L}_2 - 5\sigma_1^2\right)}, \tag{4.17a,b}$$

which secures solutions Q_2 and H_2 containing two new coefficients A_2 and B_2. Notice that (4.17) corresponds to (4.6) in the limit of $\mathscr{R}_1 \to 0$. Then Q_0, H_0, Q_1, H_1, Q_2 and H_2 are inserted into inhomogeneous terms of the next-order problem, in order to take into account viscous effects.

At $O(\epsilon^3)$, the solvability conditions of (A 7) are

$$\begin{aligned} B_2 = {} & \frac{1}{240\pi^2\left(6\mathscr{L}_2 - 5\sigma_1^2\right)\left(180\mathscr{L}_2^2 + 132\mathscr{L}_2\sigma_1^2 - 55\sigma_1^4\right)} \\ & \times \Big(60A_1\sigma_1\left(-2160\mathscr{L}_2^3 - 2484\mathscr{L}_2^2\sigma_1^2 + 275\sigma_1^6\right) \\ & + A_0\big(2^6 3^6 5\mathscr{L}_2^3\mathscr{R}_2 - 432\mathscr{L}_2^2(559\mathscr{L}_2 - 4185\mathscr{R}_2)\sigma_1^2 - 2^2 3^2 \times 5 \times 1327\mathscr{L}_2^2\sigma_1^4 \\ & + 1500(-22\mathscr{L}_2 + 45\mathscr{R}_2)\sigma_1^6 + 5^3 11 \times 23\sigma_1^8\big)\Big), \end{aligned} \tag{4.18a}$$

$$\sigma_2 = \frac{24\left(-630\mathscr{L}_2^2\mathscr{R}_2 + 3\mathscr{L}_2(-9\mathscr{L}_2 + 35\mathscr{R}_2)\sigma_1^2 + 125\mathscr{R}_2\sigma_1^4\right)}{900\mathscr{L}_2^2 + 660\mathscr{L}_2\sigma_1^2 - 275\sigma_1^4}. \tag{4.18b}$$

Here we finally see the appearance of viscous terms, plus additional interactions not present in (4.6). The solvability conditions (4.17*b*) and (4.18*b*) give the eigenvalue

$$\sigma = \overline{\sigma_1} + \overline{\sigma_2}, \tag{4.19}$$

where $\overline{\sigma_1}$ and $\overline{\sigma_2}$ satisfy

$$\overline{\sigma_1}^2 = \frac{-45\mathscr{L} - 40\pi^4\mathscr{T} \pm \sqrt{2025\mathscr{L}^2 + 6768\mathscr{L}\pi^4\mathscr{T} + 1600\pi^8\mathscr{T}^2}}{33}, \tag{4.20a}$$

$$\overline{\sigma_2} = \frac{24\left(-630\mathscr{L}^2\mathscr{R} + 3\mathscr{L}(-9\mathscr{L} + 35\mathscr{R})\overline{\sigma_1}^2 + 125\mathscr{R}\overline{\sigma_1}^4\right)}{900\mathscr{L}^2 + 660\mathscr{L}\overline{\sigma_1}^2 - 275\overline{\sigma_1}^4}. \tag{4.20b}$$

From (4.19) and (4.20), the asymptote of the Hopf_2 curve (which we denote $\mathrm{Lower}^{\mathrm{A}}$) and the corresponding neutral frequency ($|\sigma|^{\mathrm{A}}_{\mathrm{lower}}$) can be determined. We see good agreement between these predictions and solutions of (3.2) and (3.3) in figures 2(*b*,*c*) and 5(*c*). The lower-branch approximation captures the lower turning point in the neutral curve but does not connect smoothly to the upper-branch approximation, showing the need for a middle-branch approximation, given below.

https://doi.org/10.1017/jfm.2014.136 Published online by Cambridge University Press

Figure 3 shows eigenvalue paths computed from (4.19) and (4.20) and from (3.2) and (3.3), which again agree well. Equation (4.19) captures the coalescence of two pairs of conjugate eigenvalues, which takes place when

$$\mathscr{R} = \frac{11\left(\sqrt{11}-6\right)\mathscr{L}}{90\left(\sqrt{11}-11\right)} \approx 0.0427\mathscr{L}, \tag{4.21}$$

$$-\mathscr{T} = \frac{9\left(47-12\sqrt{11}\right)\mathscr{L}}{200\pi^4} \approx 0.0033\mathscr{L}; \tag{4.22}$$

the corresponding pair of eigenvalues are

$$\sigma = -\frac{\left(539-31\sqrt{11}\right)\mathscr{L}}{660} \pm \mathrm{i}\sqrt{\frac{\left(36\sqrt{11}-66\right)\mathscr{L}}{55}}. \tag{4.23}$$

The agreement between the asymptotic and numerical results can be observed in figure 3(*b*). In figure 5(*c*) we see that the coalescence point lies close to the lower turning point of the mode-2 neutral curve. As (4.23) and figure 3(*b*) indicate, when the two modes interact they are almost neutrally stable, with small decay rate of $O(\mathscr{L})$. The rapid rise in growth rate of one mode is characteristic of a 1:1 resonance. Note that the two interacting eigenmodes are each of mode-2 type, with a two-humped A_0 contribution supplemented with a smaller one-humped B_1 contribution (see (4.17*a*)).

Assuming $\mathscr{R} \sim -\mathscr{T} \ll \mathscr{L}$, the two eigenvalue components are given from (4.20*a*) and (4.20*b*) as

$$\overline{\sigma_1} = \pm 4\pi^2\mathrm{i}\sqrt{\frac{-\mathscr{T}}{15}} + \cdots, \quad \overline{\sigma_2} = -\frac{12}{125}\left(175\mathscr{R} + 8\pi^4\mathscr{T}\right) + \cdots, \tag{4.24a,b}$$

thus the real part of $\overline{\sigma}$ vanishes when

$$-\mathscr{T} = \frac{175}{8\pi^4}\mathscr{R}, \tag{4.25}$$

shown in figure 2(*a*,*b*) as Lower$^{\mathrm{L}}$, and the approximate neutral frequency is

$$\sigma = \pm 4\pi^2\mathrm{i}\sqrt{\frac{-\mathscr{T}}{15}}, \tag{4.26}$$

shown in figure 2(*c*) as $|\sigma|^{\mathrm{L}}_{\mathrm{lower}}$. Here we recover results given in XBJ for the case where the downstream rigid channel is sufficiently short to have no leading-order influence. In this case, the dominant balance in the boundary condition (3.3) at $x = 1$ is $H'' = 0$, implying zero pressure perturbation. The neutral oscillation is captured by the A_0 mode in (4.16), and does not require a contribution from the B_1 mode.

Assuming $\mathscr{L}^{3/2} \ll -\mathscr{T} \ll \mathscr{L} \ll \mathscr{R} \ll \mathscr{L}^{1/2}$, i.e. beyond the turning point of the lower-branch approximation, by balancing terms in (4.20*a*) and (4.20*b*) at increasing order, we obtain

$$\overline{\sigma_1} = \pm\mathrm{i}\sqrt{\frac{30}{11}}\mathscr{L}^{1/2} \pm \frac{16\pi^4\mathrm{i}}{5}\sqrt{\frac{6}{55}}\frac{\mathscr{T}}{\sqrt{\mathscr{L}}} + \cdots, \tag{4.27}$$

$$\overline{\sigma_2} = -\frac{6\mathscr{R}}{55} - \frac{3\mathscr{L}}{5} - \frac{2016\pi^4\mathscr{R}\mathscr{T}}{125\mathscr{L}} + \cdots. \tag{4.28}$$

https://doi.org/10.1017/jfm.2014.136 Published online by Cambridge University Press

Thus the two approximate eigenvalues are

$$\sigma = -\left(\frac{6\mathscr{R}}{55}+\frac{3\mathscr{L}}{5}+\frac{2016\pi^4\mathscr{R}\mathscr{T}}{125\mathscr{L}}\right)\pm \mathrm{i}\left(\sqrt{\frac{30}{11}}\mathscr{L}^{1/2}+\frac{16\pi^4}{5}\sqrt{\frac{6}{55}}\frac{\mathscr{T}}{\sqrt{\mathscr{L}}}\right)+\cdots, \tag{4.29}$$

which represent the overlap with the middle branch, as we see below.

4.3. *Middle branch:* $\mathscr{R}(-\mathscr{T})\sim\mathscr{L}^2$

In order to connect the upper limit of the lower branch (4.29) to the lower limit of the upper branch (4.13) and (4.14), we introduce a third region. Motivated by figure 5(*b*), we introduce the scalings

$$\mathscr{T}=\epsilon^3\mathscr{T}_3,\quad \mathscr{R}=\epsilon\mathscr{R}_1,\quad \mathscr{L}=\epsilon^2\mathscr{L}_2. \tag{4.30}$$

Here $\mathscr{T}_3$, $\mathscr{R}_1$ and $\mathscr{L}_2$ are assumed to be of order unity as $\epsilon\to 0$. Upon substituting (4.1) and (4.30) into the linearised equations (3.2) and (3.3), one homogeneous system and a series of inhomogeneous systems (see Appendix A.3) are recovered in succession.

Defining

$$\begin{aligned} f(\mathscr{R},\mathscr{L},\sigma) &= 8100\mathscr{L}\mathscr{R}^2+72\mathscr{R}\left(14\mathscr{L}+225\mathscr{R}^2\right)\sigma+30\left(\mathscr{L}+141\mathscr{R}^2\right)\sigma^2 \\ &\quad +372\mathscr{R}\sigma^3+11\sigma^4, \qquad (4.31a)\\ g_1(\mathscr{T},\mathscr{R},\sigma) &= \sigma(12\mathscr{R}+\sigma)(15\mathscr{R}+\sigma)\left(\left(1350\mathscr{R}^2+240\mathscr{R}\sigma+11\sigma^2\right)^2\right. \\ &\quad \left.-960\pi^4(15\mathscr{R}+\sigma)\mathscr{T}\right), \qquad (4.31b)\\ g_2(\mathscr{R},\sigma) &= 10\big(2^3 3^7 5^4\mathscr{R}^5+2^2 3^5 5^3 47\mathscr{R}^4\sigma+2^3 3^3 5\times 23\times 43\mathscr{R}^3\sigma^2 \\ &\quad +2^2 3^2 13\times 197\mathscr{R}^2\sigma^3+3702\mathscr{R}\sigma^4+55\sigma^5\big), \qquad (4.31c) \end{aligned}$$

using the method in previous subsections, we derive two solvability conditions $f(\mathscr{R}_1,\mathscr{L}_2,\sigma_1)=0$ and $\sigma_2=g_1(\mathscr{T}_3,\mathscr{R}_1,\sigma_1)/g_2(\mathscr{R}_1,\sigma_1)$, which give the eigenvalue

$$\sigma=\overline{\sigma_1}+\overline{\sigma_2}, \tag{4.32}$$

where $\overline{\sigma_1}$ satisfies $f(\mathscr{R},\mathscr{L},\overline{\sigma_1})=0$ and $\overline{\sigma_2}=g_1(\mathscr{T},\mathscr{R},\overline{\sigma_1})/g_2(\mathscr{R},\overline{\sigma_1})$. We can see qualitative agreement between the neutral curves and the corresponding neutral frequency determined from (4.31) and (4.32) and from the linearised equations (3.2) and (3.3) in figures 2(*b*,*c*) and 5(*b*).

Assuming $\mathscr{L}^{3/2}\ll\mathscr{T}\ll\mathscr{L}\sim\mathscr{R}^2$, by balancing terms in (4.31) at increasing order, we recover the same eigenvalues as in (4.13) and (4.14), matching the middle- and upper-branch solutions.

Assuming $\mathscr{L}^{3/2}\ll -\mathscr{T}\ll\mathscr{L}\ll\mathscr{R}\ll\mathscr{L}^{1/2}$, by balancing terms in (4.31) at increasing order we have

$$\overline{\sigma_1}=\pm\mathrm{i}\sqrt{\frac{30}{11}}\mathscr{L}^{1/2}-\frac{6\mathscr{R}}{55}+\cdots, \tag{4.33}$$

$$\overline{\sigma_2}=\pm\frac{16\pi^4\mathrm{i}}{5}\sqrt{\frac{6}{55}}\frac{\mathscr{T}}{\sqrt{\mathscr{L}}}-\frac{3\mathscr{L}}{5}-\frac{2016\pi^4\mathscr{R}\mathscr{T}}{125\mathscr{L}}+\cdots. \tag{4.34}$$

https://doi.org/10.1017/jfm.2014.136 Published online by Cambridge University Press

Thus we have two approximate eigenvalues being same as that in (4.29); thus the middle-branch solution matches onto the lower-branch solution.

As is evident from (4.31), the dominant physical balance on the middle branch is intricate and we do not attempt to pursue it further. The oscillation mechanism described in XBJ explains the behaviour at the base of the lower branch. The instability is amplified by the resonant mode interaction illustrated in figure 3. The first impact of the downstream rigid channel is to generate the lower bend in the mode-2 Hopf neutral curves. Beyond the other bend, on the upper branch of the Hopf_2 curve, there is less evidence of resonance (figure 4), but nevertheless a mode interaction generates instability. We focus now on this branch, investigating how nonlinearity influences the interaction between the two mode-2 eigenmodes.

5. Weakly nonlinear theory for the upper branch

5.1. *Derivation of amplitude equations*

Returning to the scalings used in § 4.1, we expand variables as

$$\boldsymbol{\phi}(x;\,\tau_0,\,\tau_1) = 1 + \epsilon\boldsymbol{\phi}_0 + \epsilon^2\boldsymbol{\phi}_1 + \epsilon^3\boldsymbol{\phi}_2 + \epsilon^4\boldsymbol{\phi}_3 + \cdots, \tag{5.1}$$

where $\tau_0 = \epsilon t$, $\tau_1 = \epsilon^2 t$, $\boldsymbol{\phi} \equiv (q,\,h)^{\mathrm{T}}$ and $\boldsymbol{\phi}_i \equiv (q_i,\,h_i)^{\mathrm{T}}$, $i = 0,\,1,\,2,\,3$, etc. Here τ_0, τ_1, q_i, h_i, $\mathscr{T}_2$, $\mathscr{R}_1$ and $\mathscr{L}_2$ (see (4.2)) are assumed to be of order unity as $\epsilon \to 0$.

The leading-order system is

$$q_{0x} = 0, \tag{5.2a}$$

$$6h_{0x} - 12q_{0x} + 5T_{20}h_{0xxx} = 0, \tag{5.2b}$$

$$h_0 = 0, \quad q_0 = 0 \quad (x = 0), \tag{5.2c}$$

$$h_0 = 0, \quad 12\mathscr{R}_1 q_0 + q_{0\tau_0} = 0 \quad (x = 1), \tag{5.2d}$$

and so, as in (4.3),

$$q_0 = 0, \quad h_0 = A_0 \sin 2\pi x + B_0(1 - \cos 2\pi x). \tag{5.3a,b}$$

Here A_0 and B_0 are functions of τ_0 and τ_1.

The first-order system is

$$q_{1x} = -h_{0\tau_0}, \tag{5.4a}$$

$$\begin{aligned} 6h_{1x} - 12q_{1x} + 5T_{20}h_{1xxx} = {} & -180\mathscr{R}_1 h_0 + 60\mathscr{R}_1 q_0 + 5q_{0\tau_0} \\ & - 12q_0 h_{0x} + 12h_0 q_{0x} + 12q_0 q_{0x} - 15T_{20}h_0 h_{0xxx}. \end{aligned} \tag{5.4b}$$

$$h_1 = 0, \quad q_1 = 0 \quad (x = 0), \tag{5.4c}$$

$$h_1 = 0, \quad 12\mathscr{R}_2 q_{0x} + 12\mathscr{R}_1 q_{1x} + q_{1\tau_0} + \mathscr{L}_2 T_{20} h_{0xx} = 0 \quad (x = 1). \tag{5.4d}$$

Solvability conditions for the first-order system require that

$$B_{0\tau_0} + B_0(\pi A_0 + 15\mathscr{R}_1) = 0, \tag{5.5a}$$

$$5\left(B_{0\tau_0\tau_0} + 12\mathscr{R}_1 B_{0\tau_0}\right) - 6B_0\mathscr{L}_2 = 0. \tag{5.5b}$$

This system has a divergently unstable mode for $\mathscr{R}_1 > 0$, which we suppress by enforcing $B_0 = 0$. Thus the solution of the first-order system is (cf. (4.4))

$$q_1 = A_{0\tau_0}(\cos 2\pi x - 1)/2\pi, \tag{5.6a}$$

$$\begin{aligned} h_1 = {} & A_1 \sin 2\pi x + B_1(1 - \cos 2\pi x) - \frac{A_0^2}{4}(\cos 2\pi x - \cos 4\pi x) \\ & + (15A_0\mathscr{R}_1 + A_{0\tau_0})x \sin 2\pi x. \end{aligned} \tag{5.6b}$$

https://doi.org/10.1017/jfm.2014.136 Published online by Cambridge University Press

Here A_1 and B_1 are arbitrary functions of τ_0 and τ_1. The $\sin 2\pi x$ mode appears in h_0 in (5.3), so we assume $A_1 = 0$ without loss of generality.

Solvability conditions for the second-order system require that

$$A_0(72\pi^2 B_1 - 4050\mathscr{R}_1^2 + 80\pi^4\mathscr{T}_2 - 36\pi A_{0\tau_0}) + 72\pi(15\mathscr{R}_1 B_1 + B_{1\tau_0}) = 45(\pi A_0^2(\pi A_0 + 30\mathscr{R}_1) + 8\mathscr{R}_1 A_{0\tau_0}) + 3A_{0\tau_0\tau_0}, \tag{5.7a}$$

$$\pi(9\mathscr{L}_2 A_0^2 + 10(12\mathscr{R}_1 B_{1\tau_0} + B_{1\tau_0\tau_0})) = 3(4\pi\mathscr{L}_2 B_1 + 60\mathscr{L}_2\mathscr{R}_1 A_0 + 4(\mathscr{L}_2 + 75\mathscr{R}_1^2)A_{0\tau_0} + 45\mathscr{R}_1 A_{0\tau_0\tau_0}) + 5A_{0\tau_0\tau_0\tau_0}, \tag{5.7b}$$

which generalises (4.6).

By using the original parameters $\mathscr{T}$, $\mathscr{R}$, $\mathscr{L}$, time t and defining amplitude functions $A = \epsilon A_0$, $B = \epsilon^2 B_1$, we can therefore assemble terms to give

$$h = 1 + A(t)\sin 2\pi x + B(t)(1 - \cos 2\pi x) - \frac{A(t)^2}{4}(\cos 2\pi x - \cos 4\pi x) + (15\mathscr{R}A(t) + A_t)x\sin 2\pi x + \cdots, \tag{5.8a}$$

$$q = 1 + A_t(\cos 2\pi x - 1)/2\pi + \frac{1}{8\pi^2}(60\pi\mathscr{R}A_t x\cos 2\pi x + 2\pi A(t)A_t\sin 2\pi x - 30\mathscr{R}A_t\sin 2\pi x - \pi A(t)A_t\sin 4\pi x - 8\pi^2 B_t x + 4\pi B_t\sin 2\pi x + 4\pi A_{tt}x\cos 2\pi x - 2A_{tt}\sin 2\pi x) + \cdots, \tag{5.8b}$$

where, from (5.7), the nonlinear fourth-order system governing A and B is

$$A(72\pi^2 B - 4050\mathscr{R}^2 + 80\pi^4\mathscr{T} - 36\pi A_t) + 72\pi(15\mathscr{R}B + B_t) = 45(\pi A^2(\pi A + 30\mathscr{R}) + 8\mathscr{R}A_t) + 3A_{tt}, \tag{5.9a}$$

$$\pi(9\mathscr{L}A^2 + 10(12\mathscr{R}B_t + B_{tt})) = 3(4\pi\mathscr{L}B + 60\mathscr{L}\mathscr{R}A + 4(\mathscr{L} + 75\mathscr{R}^2)A_t + 45\mathscr{R}A_{tt}) + 5A_{ttt}. \tag{5.9b}$$

The linearised system about $A = 0, B = 0$ is consistent with the quartic equation (4.8). Note that, for periodic solutions the time-averaged amplitudes satisfy (from (5.9*b*))

$$\overline{A^2} = \frac{4}{3}\overline{B} + \frac{20\mathscr{R}}{\pi}\overline{A}. \tag{5.10}$$

Thus, from (5.8*a*),

$$\overline{h(0.75, t)} - \overline{h(0.25, t)} = -\overline{A}(2 + 15\mathscr{R}), \tag{5.11}$$

indicating how time-averaged oscillations may become asymmetric about the mid-point of the membrane. We now consider some limiting cases of the amplitude equation (5.9*b*).

5.2. *Steady solutions and their stability*

For $\mathscr{L} \gg \mathscr{R}^2 \sim \mathscr{T}$, from (5.9*b*) where terms involving $\mathscr{L}$ are dominant, we recover

$$B \approx -\frac{15\mathscr{R}A}{\pi} + \frac{3A^2}{4} - \frac{A_t}{\pi}. \tag{5.12}$$

https://doi.org/10.1017/jfm.2014.136 Published online by Cambridge University Press

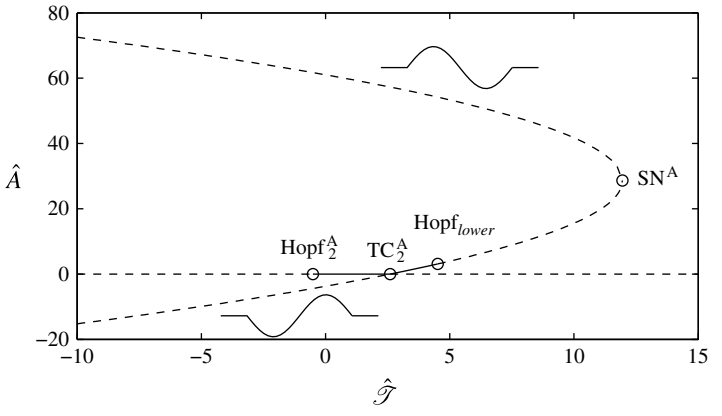


FIGURE 6. Equilibrium curves of (5.17) with $\hat{\mathscr{L}} = \mathscr{L}/\mathscr{R}^2 = 1$, where stable branches are shown by solid lines and unstable branches by dashed lines. Two insets show mode shapes.

Substituting B and B_t into (5.9*a*), we have

$$A\left(80\pi^4\mathscr{T} - 20\,250\mathscr{R}^2 + 9\pi A(\pi A - 180\mathscr{R})\right) = 2520\mathscr{R}A_t + 75A_{tt}. \tag{5.13}$$

This amplitude equation was derived by XBJ for the case $\mathscr{L} = O(1)$. This has a transcritical bifurcation (TC$_2^{\mathrm{A}}$) for

$$\mathscr{T} = 2025\mathscr{R}^2/8\pi^4 \tag{5.14}$$

and a saddle–node bifurcation (SN$^{\mathrm{A}}$) at

$$\mathscr{T} = 9315\mathscr{R}^2/8\pi^4, \tag{5.15}$$

both of which are illustrated in figure 2(*a*). The approximation TC$_2^{\mathrm{A}}$ agrees well with the numericallly predicted TC$_2$. For $\mathscr{T} < 0$ and $-\mathscr{T} \gg \mathscr{R}^2$, (5.13) is approximately Hamiltonian, with nested periodic orbits confined between $A = 0$ and two steady non-uniform solutions with $80\pi^2\mathscr{T} + 9A^2 = 0$ (XBJ). The uniform state $A = 0$ loses stability to a mode-2 equilibrium state as $\mathscr{T}$ increases through the transcritical bifurcation. These bifurcations are independent of $\mathscr{L}$ and so are shared by the full system (5.9). The steady solutions of (5.13) are indicated in the bifurcation diagram in figure 6. We now turn to oscillatory instabilities of these solutions, governed by (5.9).

We can eliminate $\mathscr{R}$ from (5.9) by rescaling as

$$\mathscr{T} = \mathscr{R}^2\hat{\mathscr{T}}, \quad \mathscr{L} = \mathscr{R}^2\hat{\mathscr{L}}, \quad t = \hat{t}/\mathscr{R}, \quad \sigma = \hat{\sigma}\mathscr{R}, \quad A = \mathscr{R}\hat{A}, \quad B = \mathscr{R}^2\hat{B}; \tag{5.16}$$

then (5.9) becomes

$$\begin{aligned}&\hat{A}\left(72\pi^2\hat{B} - 4050 + 80\pi^4\hat{\mathscr{T}} - 36\pi\hat{A}_{\hat{t}}\right) + 72\pi\left(15\hat{B} + \hat{B}_{\hat{t}}\right)\\ &\quad = 45\left(\pi\hat{A}^2(\pi\hat{A} + 30) + 8\hat{A}_{\hat{t}}\right) + 3\hat{A}_{\hat{t}\hat{t}}, \qquad (5.17a)\\ &\pi\left(9\hat{\mathscr{L}}\hat{A}^2 + 10\left(12\hat{B}_{\hat{t}} + \hat{B}_{\hat{t}\hat{t}}\right)\right)\\ &\quad = 3\left(4\pi\hat{\mathscr{L}}\hat{B} + 60\hat{\mathscr{L}}\hat{A} + 4\left(\hat{\mathscr{L}} + 75\right)\hat{A}_{\hat{t}} + 45\hat{A}_{\hat{t}\hat{t}}\right) + 5\hat{A}_{\hat{t}\hat{t}\hat{t}}. \qquad (5.17b)\end{aligned}$$

https://doi.org/10.1017/jfm.2014.136 Published online by Cambridge University Press

Using (5.17*a*), we can eliminate $\hat{A}_{\hat{t}\hat{t}}$ and $\hat{A}_{\hat{t}\hat{t}\hat{t}}$ in (5.17*b*). Thus, $\hat{A}_{\hat{t}\hat{t}}$ is the highest derivative in (5.17*a*) and $\hat{B}_{\hat{t}\hat{t}}$ is the highest derivative in (5.17*b*), allowing (5.17) to be written as a system of four first-order equations, with two parameters $\hat{\mathscr{T}}$ and $\hat{\mathscr{L}}$.

For $\hat{\mathscr{L}} \neq 0$, (5.17) has the equilibrium points $(\hat{A}, \hat{B}) = (0, 0)$ and

$$(\hat{A}_{\pm}, \hat{B}_{\pm}) = \left(\frac{270 \pm \sqrt{10}\sqrt{9315 - 8\pi^4 \hat{\mathscr{T}}}}{3\pi}, \frac{5\left(14\,985 - 8\pi^4 \hat{\mathscr{T}} \pm 48\sqrt{10}\sqrt{9315 - 8\pi^4 \hat{\mathscr{T}}}\right)}{6\pi^2} \right). \tag{5.18}$$

The equilibria (5.18) are shown in figure 6, with the transcritical bifurcation $\mathrm{TC}_2^{\mathrm{A}}$ and the saddle–node bifurcation SN^{A} arising as predicted in (5.14) and (5.15). By calculating the eigenvalues of the Jacobian matrix at these equilibria we find an additional Hopf bifurcation point $\mathrm{Hopf}_{\mathrm{lower}}$ for $(\hat{A}_-, \hat{B}_-)$ and (for sufficiently large $\hat{\mathscr{L}}$) two Hopf bifurcation points $\mathrm{Hopf}^1_{\mathrm{upper}}$ and $\mathrm{Hopf}^2_{\mathrm{upper}}$ for $(\hat{A}_+, \hat{B}_+)$. The bifurcation points are shown on figure 7(*a*). We find that $\mathrm{Hopf}^1_{\mathrm{upper}}$ emerges from SN^{A} at a Takens–Bogdanov bifurcation point when $\hat{\mathscr{L}} = 3375$ and that $\mathrm{Hopf}_{\mathrm{lower}}$ connects to $\mathrm{Hopf}^2_{\mathrm{upper}}$ on SN^{A} at a fold–Hopf bifurcation point when $\hat{\mathscr{L}} = 2^3 \times 3 \times 5 \times 23 \times 337 \approx 9.3 \times 10^5$, at which point neutral oscillations have frequency of approximately 2.5×10^6. Details are given in appendix B. We replot the corresponding bifurcation curves in $(T, \mathscr{R})$-space in figure 2(*a*) and in $(\mathscr{T}, \mathscr{R})$-space in figure 7(*b*) for $\mathscr{L} = 0.01$. For $\hat{\mathscr{L}} < 3375$, we find that steady stable states exist only for $\hat{\mathscr{T}}$ lying between $\mathrm{Hopf}_2^{\mathrm{A}}$ and $\mathrm{Hopf}_{\mathrm{lower}}$, as illustrated in figure 6.

Being fourth-order, there is potential for (5.17) to exhibit complex dynamics, which we do not aim to describe in detail here. By way of illustration, however, figure 7(*c*) shows where limit cycles emerging from $\mathrm{Hopf}_2^{\mathrm{A}}$ first undergo a period-doubling bifurcation, while figure 7(*d*) shows how subsequent period-doublings lead to apparently chaotic dynamics. Our primary interest is in the structure of the oscillations close to $\mathrm{Hopf}_2^{\mathrm{A}}$, which we now investigate in the limit in which $\hat{\mathscr{L}}$ is small. This corresponds to the upper limit of the upper branch in figure 2, where the oscillation frequency is determined primarily by the length of the downstream rigid segment.

5.3. *Oscillations arising for small* $\hat{\mathscr{L}}$

From (4.9) and (4.10), the $\mathrm{Hopf}_2^{\mathrm{A}}$ curve, plotted on figure 7, and the corresponding frequency can be re-expressed in terms of $\hat{\mathscr{T}}$ and $\hat{\mathscr{L}}$ using (5.16). Then, as $\hat{\mathscr{L}} \to 0$, the two-term approximations are

$$\hat{\mathscr{T}} = -\frac{405}{8\pi^4} + \frac{99\hat{\mathscr{L}}}{128\pi^4} + O(\hat{\mathscr{L}}^2), \tag{5.19a}$$

$$\hat{\sigma} = \pm \mathrm{i}\sqrt{\frac{27\hat{\mathscr{L}}}{8} - \frac{25\hat{\mathscr{L}}^2}{1024}} + O(\hat{\mathscr{L}}^3). \tag{5.19b}$$

Equation (5.19*a*) is illustrated in figure 7(*c*). Recall that the one-term approximations correspond to the asymptotes $\mathrm{Upper}^{\mathrm{L}}$ and $|\sigma|^{\mathrm{L}}_{\mathrm{upper}}$ in figure 2.

https://doi.org/10.1017/jfm.2014.136 Published online by Cambridge University Press

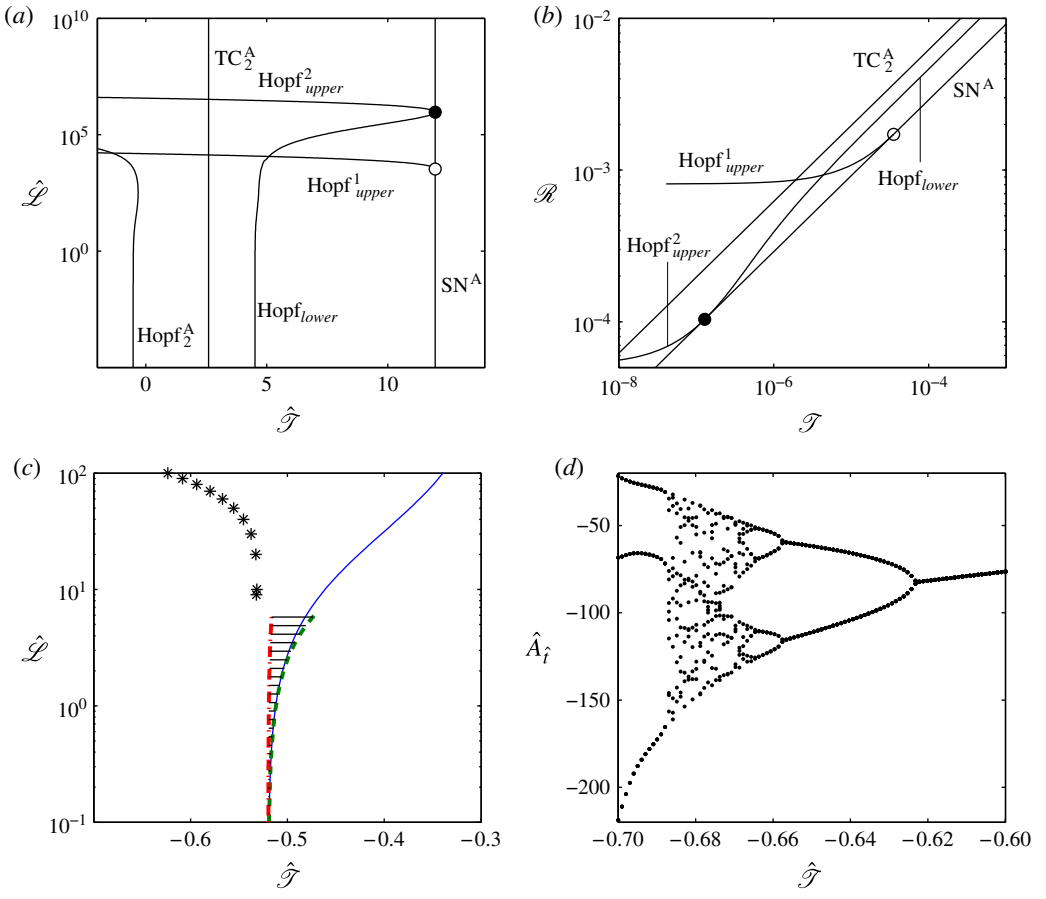


FIGURE 7. (Colour online) (*a*) Neutral curves of (5.17) in $(\hat{\mathscr{T}}, \hat{\mathscr{L}})$-space. Symbols denote the location of the fold–Hopf point at $\hat{\mathscr{L}} \approx 9.3 \times 10^5$ (solid circle) and the Takens–Bogdanov point at $\hat{\mathscr{L}} = 3375$ (open circle). (*b*) Neutral curves in $(\mathscr{T}, \mathscr{R})$-space $(\mathscr{T} > 0)$ for $\mathscr{L} = 0.01$. (*c*) Stars represent the onset of period-doubling bifurcations. Solid and dashed lines are the oscillatory neutral curve $\mathrm{Hopf}_2^{\mathrm{A}}$ and its two-term approximation given by (5.19*a*) respectively. The vertical dash-dotted line represents (C 16). The shaded region illustrates (5.29) for $\hat{\mathscr{L}} \ll 1$, within which oscillations develop sawtooth behaviour. (*d*) $\hat{A}_{\hat{t}}$ values of 10 iterations of Poincaré maps from (5.17) as $\hat{\mathscr{T}}$ changes from -0.7 to -0.6, where $\hat{\mathscr{L}} = 100$ and the Poincaré section is $\hat{A} = 0, \hat{A}_{\hat{t}} < 0$.

We now simplify (5.17) for small $\hat{\mathscr{L}}$ in the neighbourhood of the $\mathrm{Hopf}_2^{\mathrm{A}}$ curve. We rescale $\hat{A} = \hat{\mathscr{L}}^{1/2}\tilde{A}$, $\hat{B} = \hat{\mathscr{L}}^{1/2}\tilde{B}$ and introduce two time scales $\{\tilde{t}_1, \tilde{t}_2\} = \{\hat{\mathscr{L}}^{1/2}, \hat{\mathscr{L}}\}\hat{t}$. Then, motivated by (5.19*a*), we set $\hat{\mathscr{T}} = -405/8\pi^4 + \hat{\mathscr{L}}\tilde{\mathscr{T}}$ and expand

$$\tilde{A} = \tilde{A}_0 + \hat{\mathscr{L}}^{1/2}\tilde{A}_1 + \hat{\mathscr{L}}\tilde{A}_2 + \cdots, \quad \tilde{B} = \tilde{B}_0 + \hat{\mathscr{L}}^{1/2}\tilde{B}_1 + \hat{\mathscr{L}}\tilde{B}_2 + \cdots. \tag{5.20a,b}$$

Under the rescalings and expansions, (5.17) becomes a succession of amplitude equations at increasing orders in $\hat{\mathscr{L}}^{1/2}$. At $O(1)$, we have $15\tilde{A}_0 = 2\pi\tilde{B}_0$ and $15\tilde{A}_{0\tilde{t}_1} = 2\pi\tilde{B}_{0\tilde{t}_1}$, which gives $\tilde{B}_0 = 15\tilde{A}_0/(2\pi)$, indicating that the single- and double-humped modes are approximately slaved to each other.

https://doi.org/10.1017/jfm.2014.136 Published online by Cambridge University Press

At $O(\hat{\mathscr{L}}^{1/2})$, we have

$$4\pi\left(\pi\tilde{A}_0\tilde{B}_0+15\tilde{B}_1+\tilde{B}_{0\tilde{t}_1}\right) = 5\left(15\pi\tilde{A}_0^2+90\tilde{A}_1+4\tilde{A}_{0\tilde{t}_1}\right), \quad (5.21a)$$

$$3\left(60\tilde{A}_0+4\pi\tilde{B}_0+300\tilde{A}_{1\tilde{t}_1}+45\tilde{A}_{0\tilde{t}_1\tilde{t}_1}\right) = 10\pi\left(12\tilde{B}_{1\tilde{t}_1}+\tilde{B}_{0\tilde{t}_1\tilde{t}_1}\right), \quad (5.21b)$$

which gives

$$\tilde{B}_1=\frac{9\pi\tilde{A}_0^2+90\tilde{A}_1-2\tilde{A}_{0\tilde{t}_1}}{12\pi}, \quad \tilde{A}_{0\tilde{t}_1\tilde{t}_1}=-\tfrac{27}{8}\tilde{A}_0+\tfrac{9}{4}\pi\tilde{A}_0\tilde{A}_{0\tilde{t}_1}. \quad (5.22a,b)$$

At $O(\hat{\mathscr{L}})$, we have

$$\begin{aligned}&4\pi\tilde{A}_0\left(20\pi^3\tilde{\mathscr{T}}-675\tilde{A}_1+18\pi\tilde{B}_1-9\tilde{A}_{0\tilde{t}_1}\right)\\&\quad=3\Big(15\pi^2\tilde{A}_0^3+2700\tilde{A}_2-24\pi^2\tilde{A}_1\tilde{B}_0-360\pi\tilde{B}_2+120\tilde{A}_{0\tilde{t}_2}-24\pi\tilde{B}_{0\tilde{t}_2}\\&\qquad+120\tilde{A}_{1\tilde{t}_1}-24\pi\tilde{B}_{1\tilde{t}_1}+\tilde{A}_{0\tilde{t}_1\tilde{t}_1}\Big), \quad (5.23a)\\&\pi\left(9\tilde{A}_0^2+10\left(12\tilde{B}_{1\tilde{t}_2}+12\tilde{B}_{2\tilde{t}_1}+2\tilde{B}_{0\tilde{t}_1\tilde{t}_2}+\tilde{B}_{1\tilde{t}_1\tilde{t}_1}\right)\right)\\&\quad=180\tilde{A}_1+12\pi\tilde{B}_1+900\tilde{A}_{1\tilde{t}_2}+12\tilde{A}_{0\tilde{t}_1}+900\tilde{A}_{2\tilde{t}_1}\\&\qquad+270\tilde{A}_{0\tilde{t}_1\tilde{t}_2}+135\tilde{A}_{1\tilde{t}_1\tilde{t}_1}+5\tilde{A}_{0\tilde{t}_1\tilde{t}_1\tilde{t}_1}, \quad (5.23b)\end{aligned}$$

which gives

$$\begin{aligned}\tilde{B}_2 &= \big(-80\pi^4\tilde{\mathscr{T}}\tilde{A}_0-9\pi^2\tilde{A}_0^3+1620\pi\tilde{A}_0\tilde{A}_1+8100\tilde{A}_2-180\tilde{A}_{0\tilde{t}_2}\\&\quad-60\pi\tilde{A}_0\tilde{A}_{0\tilde{t}_1}-180\tilde{A}_{1\tilde{t}_1}+15\tilde{A}_{0\tilde{t}_1\tilde{t}_1}\big)/(1080\pi), \quad (5.24a)\\\tilde{A}_{0\tilde{t}_1\tilde{t}_2} &= \frac{9\pi\tilde{A}_0^2\left(35-34\pi\tilde{A}_{0\tilde{t}_1}\right)}{5120}+\frac{9\pi\tilde{A}_0\left(\tilde{A}_{0\tilde{t}_2}+\tilde{A}_{1\tilde{t}_1}\right)}{8}\\&\quad+\frac{\tilde{A}_{0\tilde{t}_1}\left(99-128\pi^4\tilde{\mathscr{T}}-42\pi\tilde{A}_{0\tilde{t}_1}\right)}{2304}-\frac{9\tilde{A}_1\left(3-2\pi\tilde{A}_{0\tilde{t}_1}\right)}{16}-\frac{\tilde{A}_{1\tilde{t}_1\tilde{t}_1}}{2}. \quad (5.24b)\end{aligned}$$

Setting $\theta(\tau)=\tilde{A}_0(\tilde{t}_1,\tilde{t}_2)+\hat{\mathscr{L}}^{1/2}\tilde{A}_1(\tilde{t}_1,\tilde{t}_2)$, with $\tilde{t}_1=\tau$ and $\tilde{t}_2=\hat{\mathscr{L}}^{1/2}\tau$, from (5.22*b*), (5.24*b*), we have, with error $O(\hat{\mathscr{L}})$,

$$\theta_{\tau\tau}+\frac{27}{8}\theta-\frac{9\pi}{4}\theta\theta_\tau=\hat{\mathscr{L}}^{1/2}\left(\frac{7\pi}{2^63}\left[\frac{27}{8}\theta^2-\theta_\tau^2\right]+\frac{\left(99-128\pi^4\tilde{\mathscr{T}}\right)}{2^73^2}\theta_\tau-\frac{153\pi^2}{2^85}\theta^2\theta_\tau\right). \quad (5.25)$$

The leading part of (5.25),

$$\theta_{\tau\tau}+\frac{27}{8}\theta-\frac{9\pi}{4}\theta\theta_\tau=0, \quad (5.26)$$

https://doi.org/10.1017/jfm.2014.136 Published online by Cambridge University Press

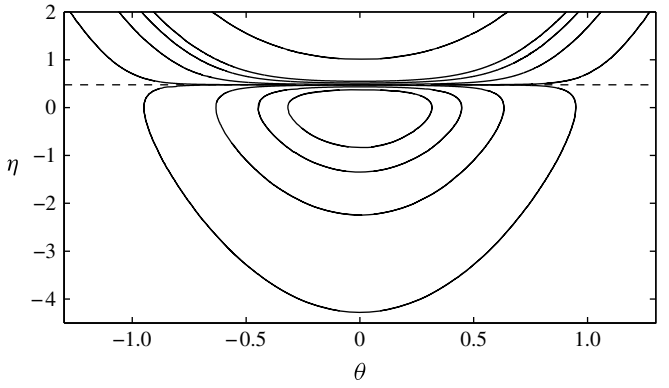


FIGURE 8. The phase portrait of (5.26). The closed orbits (moving inwards) are from (5.28) with $C=1$, 0.5, 0.3 and 0.2. The open orbits (upwards) are from (5.28) with $C=1$, 0.5, 0.3, 0.2 and -0.2. The dashed line is $\eta=3/2\pi$.

is a Liénard equation, which has the trivial solution $\theta_\tau=3/2\pi$. The substitution $\eta(\theta)=\theta_\tau$ leads to

$$\eta\eta_\theta+\frac{27}{8}\theta-\frac{9\pi}{4}\theta\eta=0, \tag{5.27}$$

which is an Abel equation of the second kind and has solution

$$\theta^2-\frac{8}{9\pi}\left(\eta+\frac{3}{2\pi}\ln\left|\eta-\frac{3}{2\pi}\right|\right)=C, \tag{5.28}$$

with integral constant C. Since $\theta=\theta(\tau)$, we use $\eta=\eta(\tau)$ in the following. The solution (5.28) represents a closed orbit and an open orbit for a fixed $C\geqslant 4\ln(2\pi/3)/3\pi^2$ (≈ 0.0999) and an open orbit for $C<4\ln(2\pi/3)/3\pi^2$ (see figure 8).

A Mel'nikov analysis (appendix C) reveals how the forcing terms on the right-hand side of (5.25) imply stability of particular orbits for different values of $\tilde{\mathscr{T}}$. The analysis confirms numerical evidence that the Hopf_2 bifurcation is supercritical and shows that a stable limit cycle grows to large amplitude as $\tilde{\mathscr{T}}\to 9/160\pi^4$ from above. Thus for

$$\frac{9\hat{\mathscr{L}}}{160\pi^4}<\hat{\mathscr{T}}+\frac{405}{8\pi^4}<\frac{99\hat{\mathscr{L}}}{128\pi^4}\quad(\hat{\mathscr{L}}\ll 1) \tag{5.29}$$

a region indicated in figure 7(*c*), oscillations are approximated by members of the family of closed orbits shown in figure 8. As the oscillations grow in amplitude, they take on a pronounced 'sawtooth' structure, with $h(0.25,\,t)\approx 1+\mathscr{L}^{1/2}\theta$ rising linearly with time (along $\theta_\tau=3/2\pi$), then falling abruptly before rising linearly again. Correspondingly the downstream constriction near $x=0.75$ opens rapidly but closes slowly. We illustrate this behaviour in more detail below through comparison with partial differential equation (PDE) simulations.

Finally, we note that for periodic solutions of (5.26), the time-average over a period satisfies $\overline{\theta}=0$ (with error $O(\hat{\mathscr{L}}^{1/2})$) by direct integration of (5.26). Multiplying (5.26) by θ and integrating again, noting the identity $\overline{\theta\theta_{\tau\tau}}+\overline{\theta_\tau^2}=0$, implies $\overline{\theta_\tau^2}=(27/8)\overline{\theta^2}$. Then, direct integration of (5.25) shows that $\overline{\theta}=0$ (with error $O(\hat{\mathscr{L}})$) even including the forcing term. Thus, given (5.11), this approximation does not predict asymmetries of time-averaged oscillations about the mid-point of the membrane.

https://doi.org/10.1017/jfm.2014.136 Published online by Cambridge University Press

6. Testing the asymptotic predictions

We now return to the full PDEs (2.2) and (2.3) to validate some of the predictions of the linear and weakly nonlinear analysis (§ 6.1). We then undertake a more stringent test of the one-dimensional model by presenting some simulations of the full two-dimensional Navier–Stokes problem (§ 6.2). In comparing one-dimensional asymptotics to the one-dimensional PDE, discrepancies may arise because the parameters $\mathscr{R}$, $\mathscr{T}$ and $\mathscr{L}$ are not sufficiently close to zero; in comparing the one-dimensional and two-dimensional models, we cannot expect quantitative agreement with the one-dimensional model as the one-dimensional model is derived on the basis of some *ad hoc* assumptions.

6.1. *One-dimensional simulations*

Using the method given in Appendix E of XBJ, we perform numerical simulations of the one-dimensional model (2.2) and (2.3) for parameter values near the Hopf_2 and TC_2 bifurcations points, as indicated by the crosses in figure 2(*a*). We again write $T = T_{20} + \hat{\mathscr{T}}\mathscr{R}^2$, fix $\mathscr{R} = 0.01$ and $\mathscr{L} = 0.01$ and use the initial condition $h = 1 + A_{init}\sin 2\pi x$ with $A_{init} = 0.01$.

Figure 9 shows, for $\hat{\mathscr{T}} = -0.7$ and -0.75 (the two crosses near $\mathrm{Upper}^{\mathrm{L}}$ in figure 2(*a*) are almost indistinguishable), that a mode-2 oscillatory instability arises from the uniform steady state as expected, to yield a sustained mode-2 sawtooth oscillation. The oscillation shown in figure 9(*a*,*b*) has period of ∼40, which is close to the predicted period 37 of the neutral oscillation at the nearby Hopf bifurcation point (see (4.10)). While the trajectory for $\hat{\mathscr{T}} = -0.7$ has a characteristic shape similar to the sawtooth orbits in figure 8, the slight asymmetry $\overline{h(0.75, t)} > \overline{h(0.25, t)}$ evident in the simulation is not predicted by (5.25) (which assumes $\hat{\mathscr{L}} \ll 1$). Slightly decreasing T, we see period-doubling in figure 9(*b*), which agrees qualitatively with the prediction from the fourth-order amplitude equation (5.17) (see figure 7*c*). For these parameter values, $\hat{\mathscr{L}} = 100$ and period-doubling is predicted for $\hat{\mathscr{T}} \approx -0.6236$ via asymptotics (figure 7*c*), whereas the PDE results indicate that it lies in the interval $(-0.75, -0.7)$.

Figure 10 shows simulations for parameter values near TC_2 and $\mathrm{Hopf}_{\mathrm{lower}}$ (see the crosses on figure 2*a*). For $\hat{\mathscr{T}} = 5$, linear stability analysis suggests that the uniform steady state should be destabilised by divergent instability (see figures 6, 7*a*), which is confirmed by the PDE simulation shown in figure 10(*a*). The simulation predicts that the uniform steady state finally goes to a mode-2 steady state. In contrast, for $\hat{\mathscr{T}} = 6.4$ in figure 10(*b*), the uniform state is divergently unstable before going to a small-amplitude oscillation about the mode-2 steady state. Thus the simulations provide evidence for the existence of $\mathrm{Hopf}_{\mathrm{lower}}$, placing it in the range $5 < \hat{\mathscr{T}} < 6.4$, whereas the weakly nonlinear analysis predicts that it lies at $\hat{\mathscr{T}} \approx 4.6343$ for these values of $\mathscr{L}$ and $\mathscr{R}$ (see (B 3)).

6.2. *Two-dimensional simulations*

In the two-dimensional numerical simulations, obtained using the method outlined in § 2, we fix $L_1 = 5$, $L = 10$, $L_2 = 100$ (so that $\mathscr{L} = 0.1$), and $\mathscr{R} = 0.01$. These parameters comfortably satisfy the constraints given in § 2 for membrane stretching and bending effects to be weak. To investigate the evolution of the system, as in Stewart *et al.* (2010), we firstly slightly perturb the linear external pressure supporting the uniform

https://doi.org/10.1017/jfm.2014.136 Published online by Cambridge University Press

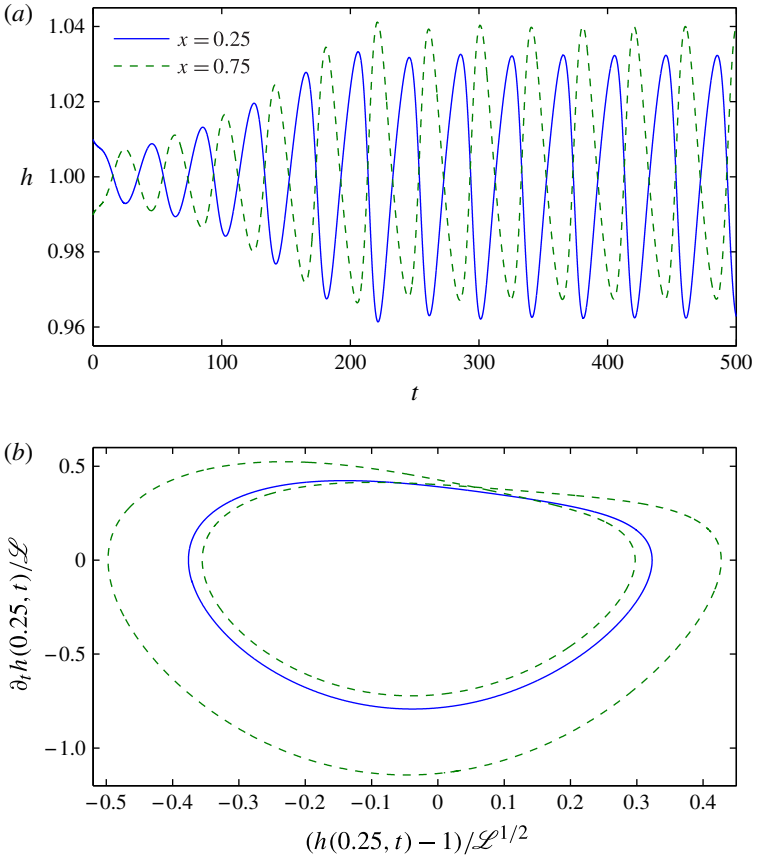


FIGURE 9. (Colour online) Simulations of the one-dimensional model (2.2) and (2.3) for $\mathscr{R} = 0.01$ and $\mathscr{L} = 0.01$ ($\hat{\mathscr{L}} = 100$). (*a*) The time trace of membrane displacements at $x = 0.25$ and $x = 0.75$ for $\hat{\mathscr{T}} = -0.7$; the out-of-phase motion is characteristic of a mode-2 oscillation. (*b*) The final limit cycle represented by $h(0.25, t) - 1$ scaled by $\mathscr{L}^{1/2}$ and its time derivative scaled by $\mathscr{L}$ for $\hat{\mathscr{T}} = -0.7$ (solid) and for $\hat{\mathscr{T}} = -0.75$ (dashed).

state, to get a steady state with a slightly deformed membrane shape. Then we use the steady state as the initial condition for the unsteady simulation. We undertook grid convergence studies in order to ensure that predictions were accurate; in order to avoid a grid-scale instability in the downstream segment, for the initial guess we used a coarse structured grid which was then refined adaptively.

For these parameters, we find that a Hopf bifurcation (resembling Hopf_2) is located in the range $0.017 < T < 0.018$, whereas the linear stability analysis of the one-dimensional model predicts that Hopf_2 lies at $T \approx 0.03004$ for these values of $\mathscr{R}$ and $\mathscr{L}$ (figure 2*a*). Deceasing T, sawtooth oscillations (characteristic of the upper branch of the Hopf_2 curve) are seen when $T = 0.0167$ (figure 11*a*). For these oscillations, the pressure and flux at $x = 1$ are slightly out of phase, with pressure ahead of the flux. The supplementary movie (available at http://dx.doi.org/10.1017/jfm.2014.136) illustrates the structure of the internal flow field, which shows minimal evidence of flow separation or of disturbances propagating into the downstream segment. In this example, the downstream constriction opens within 30 % of the total oscillation period.

https://doi.org/10.1017/jfm.2014.136 Published online by Cambridge University Press

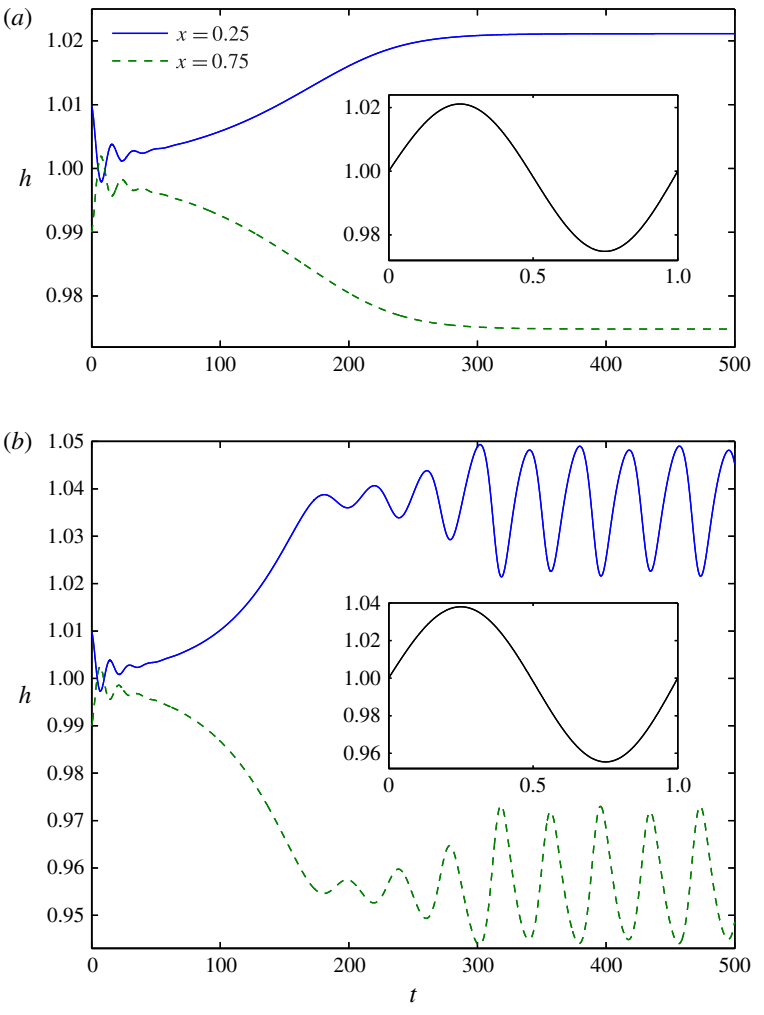


FIGURE 10. (Colour online) Simulations of the one-dimensional model (2.2) and (2.3) for $\mathscr{R} = 0.01$ and $\mathscr{L} = 0.01$. The time trace of the membrane displacements at $x = 0.25$ and $x = 0.75$ for $\hat{\mathscr{T}} = 5$ (*a*) and $\hat{\mathscr{T}} = 6.4$ (*b*). The insets show the shape of the corresponding mode-2 steady solutions.

Figure 11(*b*) shows that the limit cycle resembles the orbits shown in figure 8 but becomes distorted as T decreases further; period doubling was not observed. Instead, as T is reduced to 0.0163, the system goes to a mode-1 (inflated) steady state rather than a stable limit cycle (figure 11*c*). In this example, we can see a few transient sawtooth oscillations increasing in amplitude and period, with 'ringing' taking place when the tube opens abruptly at its downstream end.

Figure 12 shows similar behaviour to figure 10, but for $T = 0.03$ (resembling the case of $\hat{\mathscr{T}} = 5$) and $T = 0.0315$ (resembling the case of $\hat{\mathscr{T}} = 6.4$), which suggests that the analogue of $\mathrm{Hopf}_{\mathrm{lower}}$ exists in the range $0.03 < T < 0.0315$. We also find a transcricritical bifurcation point resembling TC_2 in the range $0.024 < T < 0.026$, whereas the linear stability analysis of the one-dimensional model predicts that TC_2 lies at $T \approx 0.03071$ for the value of $\mathscr{R}$ (figure 2*a*).

https://doi.org/10.1017/jfm.2014.136 Published online by Cambridge University Press

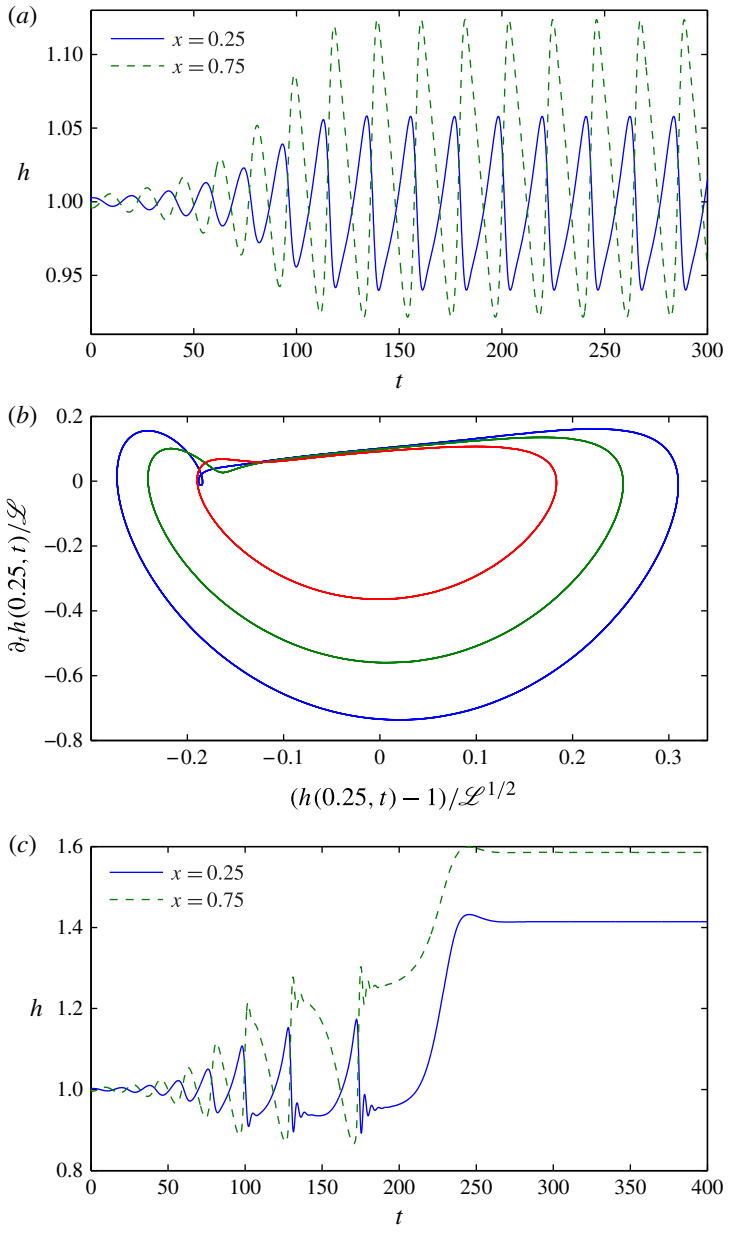


FIGURE 11. (Colour online) Two-dimensional simulations for $\mathscr{R} = 0.01$ and $\mathscr{L} = 0.1$. (*a*) The time trace of the channel width at $x = 0.25$ and $x = 0.75$ for $T = 0.0167$. (*b*) The final limit cycle for $T = 0.0167$, 0.0165, 0.0164 (with amplitude increasing as T falls). (*c*) The time trace of the channel width at $x = 0.25$ and $x = 0.75$ for $T = 0.0163$.

7. Discussion

There have been numerous experimental studies demonstrating the importance of the conditions downstream of a flexible tube in determining the characteristics of self-excited oscillations (Wang, Chew & Low 2009; Heil & Hazel 2011); for the two-dimensional analogue system (figure 1), however, we must rely instead on numerical

https://doi.org/10.1017/jfm.2014.136 Published online by Cambridge University Press

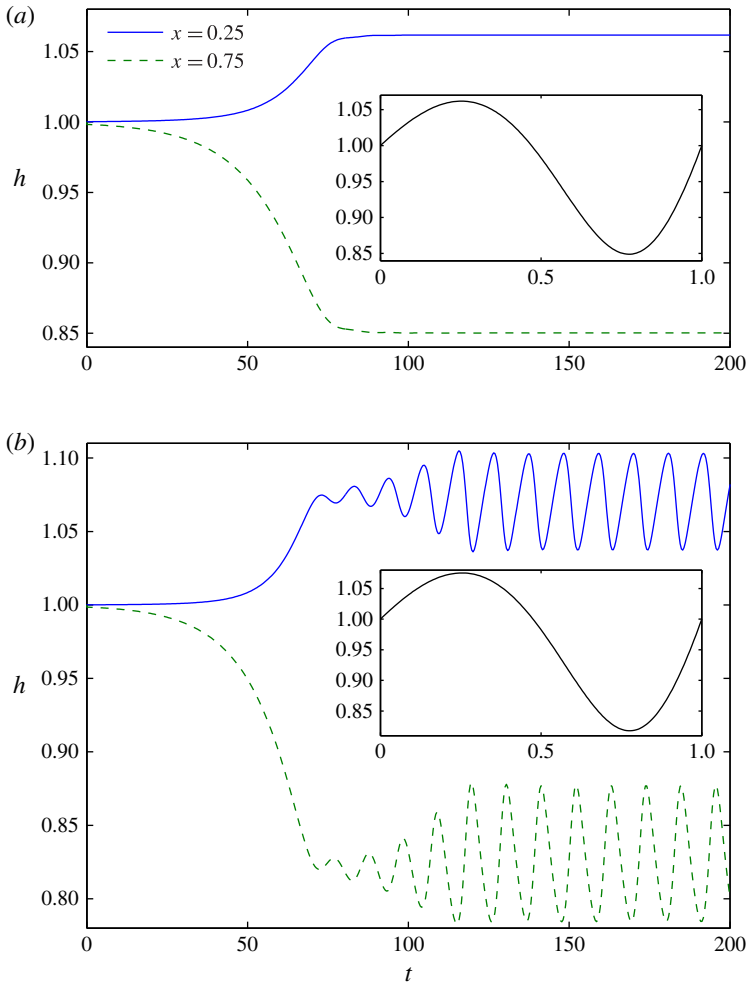


FIGURE 12. (Colour online) Two-dimensional simulations for $\mathscr{R} = 0.01$ and $\mathscr{L} = 0.1$. The time trace of the channel width at $x = 0.25$ and $x = 0.75$ for $T = 0.03$ (a) and 0.0315 (b). The insets are the shape of the corresponding mode-2 steady solutions.

simulations for empirical data. Often the resistance and inertia of the downstream part of the system have been manipulated independently through the use of valves, whereas in the present model the two effects are coupled through the parameter L_2 (for a flow at a given Reynolds number). Whereas Bertram & Butcher (1992) found little evidence that the frequency of oscillations is entrained to the resonant frequency of the downstream system (in the manner characteristic of a musical wind instrument), Bertram & Tscherry (2006) reported that increasing the length of the downstream tube reduced the frequency of oscillations but had little effect on the conditions for onset. This is mirrored in our model by oscillations arising along the upper end of the upper branch of the Hopf_2 curve (see (4.11) and (4.12)), with frequency of magnitude $q_0/a\sqrt{L^* L_2^*}$ and onset Reynolds number (4.11) that is independent of L_2^*, suggesting a possible mechanistic connection with their observations.

By exploring a one-dimensional model of an idealised two-dimensional physical system, we have been able to understand in detail the conditions leading to instability,

https://doi.org/10.1017/jfm.2014.136 Published online by Cambridge University Press

and the role played by the downstream rigid channel. We have explored the neighbourhood of an organising centre in parameter space, in the hope that it presents a microcosm of the broader range of possible behaviour, while still being accessible to asymptotic analysis. The singular point we have investigated is one at which the inviscid problem admits neutrally stable wave-like disturbances arising via the Bernoulli effect; analogous bifurcation points were identified independently by Guneratne & Pedley (2006) using a two-dimensional model based on interactive boundary-layer theory. Two types of membrane perturbation arise: a two-humped $\sin(2\pi x)$ disturbance, made slightly asymmetric by viscous and convective inertia effects; and a single-humped $(1 - \cos(2\pi x))$ mode. These modes have similar frequency and the same wavelength, promoting their interaction. Because the inlet flux is fixed, coupling between these modes arises through axial sloshing motions induced in the downstream rigid segment. Since the odd (one-humped) disturbance induces stronger sloshing than the even (two-humped) one, when the modes are coupled the former has smaller amplitude than the latter.

We have identified three important classes of behaviour: low-frequency transiently growing oscillations (arising along the lower branch of the Hopf_2 curve), that are largely independent of L_2 (see figure 2*b*,*c*) but are driven by divergent instabilities of nearby saddle points (for details see XBJ); a 1:1 resonance (figure 3*b*), mediated by L_2, leading to an abrupt bend in the Hopf_2 curve (see figure 5*c*, where the lower branch of the Hopf_2 curve joins the middle branch); and higher-frequency (yet still slow) oscillations involving a weak sloshing motion in the downstream rigid tube, arising along the upper branch of the Hopf_2 curve (see figure 5*a*). The membrane deflection is described in terms of amplitudes A and B in (5.8*a*). The resulting oscillations arise at moderate Reynolds numbers (figure 2*a*) and can saturate to give stable limit cycles (figure 7*d*).

By performing a three-parameter unfolding of the degenerate bifurcation, we have derived a fourth-order equation (5.17) for the amplitudes A and B, itself having two independent parameters, describing behaviour in a neighbourhood of the organising centre, which captures the upper branch of the Hopf_2 curve. These equations describe the coupled evolution of the one- and two-humped modes. We have not attempted to classify the full properties of (5.17), but instead have focused on a few prominent features. First, in addition to the primary Hopf instability of the uniform state, (5.17) predicts an additional Hopf bifurcation of a non-uniform steady state ($\mathrm{Hopf}_{\mathrm{lower}}$ in figures 6 and 7*a*). We had previously seen an indication of such a bifurcation (see figure 5*c* of XBJ), arising even when $L_2 = 1$, indicating that the behaviour we report need not be restricted to the limit $L_2 \gg 1$ but nevertheless involves coupling with the downstream rigid channel. Second, the oscillations arising from the uniform state develop a characteristic sawtooth structure as they grow in amplitude (see figure 8 and the supplementary movie), for which the constriction near the downstream end of the membrane opens rapidly but closes slowly. We have validated both of these asymptotic predictions by comparison with PDE simulations of the full one-dimensional model (2.2) and (2.3), as shown in figures 9 and 10.

In a much more stringent test of these predictions, we have also replicated sawtooth oscillations using full two-dimensional Navier–Stokes simulations (figure 11). This provides reassuring justification for our detailed study of the one-dimensional model, as well as demonstrating the robustness of its predictions in this regime of parameter space. Because we are investigating small-amplitude low-frequency oscillations in a slender domain, the internal axial velocity profile remains roughly parabolic without undergoing significant flow reversal (see the supplementary movie); these are

https://doi.org/10.1017/jfm.2014.136 Published online by Cambridge University Press

conditions under which the one-dimensional model might be expected to provide an effective approximation, even at moderately high Reynolds numbers. However some predictions of the one-dimensional model that are particularly sensitive to parameters, such as a period-doubling cascade (figures 7*a* and 9*b*) may not be expected to be robust, particularly as amplitudes grow and time-scales fall. Further computational studies, in both two and three dimensions and with a wider range of wall models, will therefore be needed to assess the wider relevance of the instability mechanisms identified here.

Finally, it is useful to translate the asymptotic threshold (4.11) for the onset of upper-branch oscillations back to the original dimensional variables. First, the Hopf_2 curve, demarking the primary oscillatory instability of the uniform state, lies in $T < T_{20}$, which is equivalent to

$$Re > \left(\frac{10\pi^2}{3}\right)^{1/2} \left(\frac{\rho T_0 a}{\mu^2}\right)^{1/2} \frac{a}{L^*}, \tag{7.1}$$

where $Re = \rho q_0/\mu$. This threshold provides a necessary condition for the existence of upper-branch oscillations; the analysis presented here is valid close to this threshold. In particular, the sawtooth oscillations, that are anticipated to arise when oscillations become weakly nonlinear, exist close to the threshold

$$Re^2 \approx \frac{10\pi^2}{3} \left(\frac{\rho T_0 a}{\mu^2}\right) \frac{a^2}{L^{*2}} + \frac{675\pi^4}{4} \frac{L^{*2}}{a^2} \ll \frac{L_2^* L^*}{a^2}. \tag{7.2}$$

Equation (7.2) includes (4.11) plus the constraint $\mathscr{R}^2 \gg \mathscr{L}$. For this asymptotic approximation to be valid, the L^{*2}/a^2 term, while numerically large, must provide a relatively small correction to the primary estimate (7.1), while the downstream length must be sufficiently long to suppress features associated with the middle and lower branches of the Hopf_2 curve. In contrast, the corresponding threshold for 'sloshing' oscillations under pressure–pressure boundary conditions is $Re \sim (\rho T_0 a/\mu^2)^{1/4}$ (Jensen & Heil 2003) (provided the length L_1^* of the upstream rigid channel segment is sufficiently less than L_2^*), which lies below (7.1) when (7.2) is valid. It is notable that the stationary eigenmodes arising at $\mathscr{R} = 0$, $T = T_{n0}$ exist also when the upstream pressure is prescribed, in which case the present study is equivalent to taking the limit of very large L_1. It would therefore be of interest in future studies to relax this condition to explore possible interactions between mode-1 sloshing and mode-2 upper-branch instabilities.

Acknowledgement

We are grateful to Professor Matthias Heil for his generous advice in implementing oomph-lib.

Supplementary movie

A supplementary movie is available at http://dx.doi.org/10.1017/jfm.2014.136.

Appendix A. Parametric expansions

A.1. *Upper branch*

Upon substituting (4.1) and (4.2) into the linearised equations (3.2) and (3.3), one homogeneous system and a series of inhomogeneous systems are recovered in succession.

https://doi.org/10.1017/jfm.2014.136 Published online by Cambridge University Press

At $O(1)$, we obtain

$$Q_0' = 0, \tag{A 1a}$$
$$6H_0' - 12Q_0' + 5T_{20}H_0''' = 0, \tag{A 1b}$$
$$H_0 = Q_0 = 0 \quad (x = 0), \tag{A 1c}$$
$$H_0 = 0, \quad (12\mathscr{R}_1 + \sigma_1)Q_0 = 0 \quad (x = 1). \tag{A 1d}$$

At $O(\epsilon)$, we obtain

$$Q_1' = -\sigma_1 H_0, \tag{A 2a}$$
$$6H_1' - 12Q_1' + 5T_{20}H_1''' = -(180\mathscr{R}_1 H_0 - 60\mathscr{R}_1 Q_0 - 5\sigma_1 Q_0), \tag{A 2b}$$
$$H_1 = Q_1 = 0 \quad (x = 0), \tag{A 2c}$$
$$H_1 = 0, \quad (12\mathscr{R}_1 + \sigma_1)Q_1 = -(\sigma_2 Q_0 + \mathscr{L}_2 T_{20} H_0'') \quad (x = 1). \tag{A 2d}$$

At $O(\epsilon^2)$, we obtain

$$Q_2' = -(\sigma_2 H_0 + \sigma_1 H_1), \tag{A 3a}$$
$$6H_2' - 12Q_2' + 5T_{20}H_2''' = -(180\mathscr{R}_1 H_1 - 60\mathscr{R}_1 Q_1 - 5\sigma_2 Q_0 - 5\sigma_1 Q_1 + 5\mathscr{T}_2 H_0'''), \tag{A 3b}$$
$$H_2 = Q_2 = 0 \quad (x = 0), \tag{A 3c}$$
$$H_2 = 0, \quad (12\mathscr{R}_1 + \sigma_1)Q_2 = -(\sigma_3 Q_0 + \sigma_2 Q_1 + \mathscr{L}_2 T_{20} H_1'') \quad (x = 1). \tag{A 3d}$$

To solve these linear boundary value problems, we obtain the general solutions with four undetermined coefficients; then we substitute the general solutions into boundary conditions, which leads to a linear system of algebraic equations (homogeneous or inhomogeneous) with four unknowns. The resultant algebraic system for (A 1) is under-determined and its solution exists unconditionally. For the inhomogeneous systems (A 2) and (A 3), we impose solvability conditions following the approach given in XBJ. The same method is used for the lower and middle branches in the following and the weakly nonlinear analysis for the upper branch in § 5.

A.2. *Lower branch*

Upon substituting (4.1) and (4.15) into the linearised equations (3.2) and (3.3), one homogeneous system and a series of inhomogeneous systems are recovered in succession.

At $O(1)$, we obtain (A 1*a–c*) with

$$H_0 = 0, \quad \sigma_1 Q_0 = 0 \quad (x = 1). \tag{A 4}$$

At $O(\epsilon)$, we obtain (A 2*a*,*c*) with

$$6H_1' - 12Q_1' + 5T_{20}H_1''' = 5\sigma_1 Q_0, \tag{A 5a}$$
$$H_1 = 0, \quad \sigma_1 Q_1 = -((12\mathscr{R}_2 + \sigma_2)Q_0 + \mathscr{L}_2 T_{20} H_0'') \quad (x = 1). \tag{A 5b}$$

At $O(\epsilon^2)$, we obtain (A 3*a–c*) with

$$H_2 = 0, \quad \sigma_1 Q_2 = -(\sigma_3 Q_0 + (12\mathscr{R}_2 + \sigma_2)Q_1 + \mathscr{L}_2 T_{20} H_1'') \quad (x = 1). \tag{A 6}$$

https://doi.org/10.1017/jfm.2014.136 Published online by Cambridge University Press

At $O(\epsilon^3)$, we obtain

$$Q_3' = -(\sigma_3 H_0 + \sigma_2 H_1 + \sigma_1 H_2), \tag{A 7a}$$

$$6H_3' - 12Q_3' + 5T_{20}H_3''' = -(180\mathscr{R}_2 H_1 - 5\sigma_3 Q_0 - 60\mathscr{R}_2 Q_1 - 5\sigma_2 Q_1 - 5\sigma_1 Q_2 + 5\mathscr{T}_2 H_1'''), \tag{A 7b}$$

$$H_3 = Q_3 = 0 \quad (x = 0), \tag{A 7c}$$

$$H_3 = 0, \quad \sigma_1 Q_3 = -(\sigma_4 Q_0 + \sigma_3 Q_1 + (12\mathscr{R}_2 + \sigma_2)Q_2 + \mathscr{L}_2\mathscr{T}_2 H_0'' + \mathscr{L}_2 T_{20} H_2'') \quad (x = 1). \tag{A 7d}$$

A.3. *Middle branch*

Upon substituting (4.1) and (4.30) into the linearised equations (3.2) and (3.3), one homogeneous system and a series of inhomogeneous systems are recovered in succession. At $O(1)$, we obtain (A 1*a–d*). At $O(\epsilon)$, we obtain (A 2*a–d*). At $O(\epsilon^2)$, we obtain (A 3*a*,*c*,*d*) and

$$6H_2' - 12Q_2' + 5T_{20}H_2''' = -(180\mathscr{R}_1 H_1 - 60\mathscr{R}_1 Q_1 - 5\sigma_2 Q_0 - 5\sigma_1 Q_1). \tag{A 8}$$

At $O(\epsilon^3)$, we obtain (A 7*a*,*c*) and

$$6H_3' - 12Q_3' + 5T_{20}H_3''' = -(180\mathscr{R}_1 H_2 - 60\mathscr{R}_1 Q_2 - 5\sigma_3 Q_0 - 5\sigma_2 Q_1 - 5\sigma_1 Q_2 + 5\mathscr{T}_3 H_0'''), \tag{A 9a}$$

$$H_3 = 0, \quad (12\mathscr{R}_1 + \sigma_1)Q_3 = -(\sigma_4 Q_0 + \sigma_3 Q_1 + \sigma_2 Q_2 + \mathscr{L}_2 T_{20} H_2'') \quad (x = 1). \tag{A 9b}$$

Appendix B. Hopf bifurcation along the non-uniform branches

For the equilibrium point $(\hat{A}_-, \hat{B}_-)$, the eigenvalue $\hat{\sigma}$ satisfies

$$24\hat{\mathscr{L}}b\big(27\sqrt{10} - b\big) + 48\big(5b\big(297\sqrt{10} - 5b\big) + 63(\hat{\mathscr{L}} - 3375)\big)\hat{\sigma} + 10\big(2b\big(297\sqrt{10} - 5b\big) + 9(\hat{\mathscr{L}} - 9354)\big)\hat{\sigma}^2 + 1116\hat{\sigma}^3 + 33\hat{\sigma}^4 = 0, \tag{B 1}$$

where $b \equiv \sqrt{9315 - 8\pi^4\hat{\mathscr{T}}}$ $(\geqslant 0)$. If $\hat{\sigma} = \mathrm{i}\omega$, for ω non-zero and real, then

$$\omega^2 = 2 \times 3^2 \times 5 \times 7 \times 1993 - \frac{4b\big(6264\sqrt{10} - 97b\big)}{3} + 2\sqrt{3^4 5^2 7^2 1993^2 + \frac{4b\Delta_{\text{lower}}}{3}}, \tag{B 2}$$

when $(b, \hat{\mathscr{L}})$ lies on the oscillatory neutral curve $\mathrm{Hopf}_{\text{lower}}$

$$\hat{\mathscr{L}} = \frac{3^3 \times 5 \times 7 \times 62\ 233 - 2b\big(3^3 \times 7247\sqrt{10} - 3032b\big) + 31\sqrt{3^6 5^2 7^2 1993^2 + 12b\Delta_{\text{lower}}}}{126}, \tag{B 3}$$

where $\Delta_{\text{lower}} \equiv -3^5 \times 5 \times 7 \times 47 \times 9833\sqrt{10} + 2b(3^2 \times 5 \times 59 \times 36\,061 - 4b(2^4 3^5 13\sqrt{10} - 391b))$. When $b = 0$, that is $\hat{\mathscr{T}} = 9315/8\pi^4$, the $\mathrm{Hopf}_{\text{lower}}$ curve merges with the SN^{A} curve at $\hat{\mathscr{L}} = 2^3 \times 3 \times 5 \times 23 \times 337$, as seen in figure 7(*a*), which suggests a fold–Hopf bifurcation. At the fold–Hopf bifurcation point, the equilibrium has a zero eigenvalue and a pair of purely imaginary eigenvalues $\hat{\sigma} = \pm 2^2 3^2 \times 5 \times 7 \times 1993\mathrm{i}$. Figure 7(*a*) also shows that the $\mathrm{Hopf}_{\text{lower}}$ curve lies along $\hat{\mathscr{T}} \approx 4.5129$ when $\hat{\mathscr{L}} \ll 1$.

https://doi.org/10.1017/jfm.2014.136 Published online by Cambridge University Press

For the equilibrium point $(\hat{A}_+, \hat{B}_+)$, the eigenvalue $\hat{\sigma}$ satisfies

$$-24\hat{\mathscr{L}}b\big(27\sqrt{10}+b\big)-48\big(5b\big(297\sqrt{10}+5b\big)-63(\hat{\mathscr{L}}-3375)\big)\hat{\sigma}$$
$$-10\big(2b\big(297\sqrt{10}+5b\big)-9(\hat{\mathscr{L}}-9354)\big)\hat{\sigma}^2+1116\hat{\sigma}^3+33\hat{\sigma}^4=0. \tag{B 4}$$

From (B 4), the non-zero frequency ω satisfies

$$\omega^2=2\times3^2\times5\times7\times1993+\frac{4b\big(6264\sqrt{10}+97b\big)}{3}\mp2\sqrt{3^4 5^2 7^2 1993^2+\frac{4b\Delta_{\text{upper}}}{3}}, \tag{B 5}$$

on the oscillatory neutral curve $\text{Hopf}^1_{\text{upper}}/\text{Hopf}^2_{\text{upper}}$

$$\hat{\mathscr{L}}=\frac{3^3\times5\times7\times62\,233+2b\big(3^3\times7247\sqrt{10}+3032b\big)\mp31\sqrt{3^6 5^2 7^2 1993^2+12b\Delta_{\text{upper}}}}{126}, \tag{B 6}$$

where $\Delta_{\text{upper}}\equiv-3^5\times5\times7\times47\times9833\sqrt{10}+2b(3^2\times5\times59\times36061-4b(2^4 3^5 13\sqrt{10}-391b))$. The $\text{Hopf}^1_{\text{upper}}$ curve originates from a Takens–Bogdanov bifurcation point with double-zero eigenvalues located on the SN^{A} curve when $\hat{\mathscr{L}}=3375$. The $\text{Hopf}^2_{\text{upper}}$ curve smoothly connects to the $\text{Hopf}_{\text{lower}}$ through the fold–Hopf bifurcation point. These curves are shown in figure 7(*a*).

Appendix C. Mel'nikov analysis

The perturbed system (5.25) can be rewritten as $(\theta_\tau, \eta_\tau)^{\text{T}}=\boldsymbol{f}(\theta,\eta)+\epsilon\boldsymbol{g}\big(\theta,\eta,\tilde{\mathscr{T}}\big)$, where $\epsilon=\hat{\mathscr{L}}^{1/2}(\ll1)$ and

$$\boldsymbol{f}=\left(\eta,\frac{9\pi}{4}\theta\eta-\frac{27}{8}\theta\right)^{\text{T}}, \tag{C 1a}$$

$$\boldsymbol{g}=\left(0,\frac{63\pi}{2^9}\theta^2+\frac{\big(99-128\pi^4\tilde{\mathscr{T}}\big)}{2^7 3^2}\eta-\frac{153\pi^2}{2^8 5}\theta^2\eta-\frac{7\pi}{2^6 3}\eta^2\right)^{\text{T}}. \tag{C 1b}$$

The unperturbed system, i.e. $\epsilon=0$, has a one-parameter family of periodic orbits $\big(\theta^C(\tau),\eta^C(\tau)\big)$, $C\in(4\ln(2\pi/3)/3\pi^2,\infty)$ and corresponding period T^C.

The Mel'nikov function (Holmes 1980, XBJ) for the perturbed system along the cycle $\big(\theta^C(\tau),\eta^C(\tau)\big)$ of period T^C of the unperturbed system is given by

$$M(C,\tilde{\mathscr{T}})=\int_0^{T^C}\exp\left[-\int_0^\tau\boldsymbol{\nabla}\cdot\boldsymbol{f}\left(\theta^C(s),\eta^C(s)\right)\mathrm{d}s\right]$$
$$\times\boldsymbol{f}(\theta^C(\tau),\eta^C(\tau))\wedge\boldsymbol{g}(\theta^C(\tau),\eta^C(\tau),\tilde{\mathscr{T}})\mathrm{d}\tau. \tag{C 2}$$

We evaluate the exponential part of the integrand in the Mel'nikov function, using (5.26), as

$$\exp\left[-\int_0^\tau\boldsymbol{\nabla}\cdot\boldsymbol{f}\left(\theta^C(s),\eta^C(s)\right)\mathrm{d}s\right]=\exp\left[-\frac{9\pi}{4}\int_0^\tau\theta^C(s)\mathrm{d}s\right]$$
$$=\exp\left[-2\pi\int_0^\tau\frac{\theta^C_{ss}}{2\pi\theta^C_s-3}\mathrm{d}s\right]$$
$$=\frac{3-2\pi\theta_\tau(0)}{3-2\pi\theta_\tau(\tau)}=\frac{3-2\pi\eta(0)}{3-2\pi\eta(\tau)}. \tag{C 3}$$

https://doi.org/10.1017/jfm.2014.136 Published online by Cambridge University Press

The wedge product in the integrand is

$$\begin{aligned}&\boldsymbol{f}(\theta^C(\tau),\eta^C(\tau))\wedge\boldsymbol{g}(\theta^C(\tau),\eta^C(\tau),\tilde{\mathscr{T}})\\&\quad=\eta\left(\frac{63\pi}{2^9}\theta^2+\frac{\left(99-128\pi^4\tilde{\mathscr{T}}\right)}{2^7 3^2}\eta-\frac{153\pi^2}{2^8 5}\theta^2\eta-\frac{7\pi}{2^6 3}\eta^2\right).\end{aligned}\tag{C 4}$$

Then the condition of periodic orbits of the unperturbed system being preserved under small perturbations, $M(C,\tilde{\mathscr{T}})=0$, becomes

$$\int_0^{T^C}\frac{\eta(20\eta(-99+128\pi^4\tilde{\mathscr{T}}+42\pi\eta)+81\pi(-35+34\pi\eta)\theta^2)}{23\,040(-3+2\pi\eta)}\mathrm{d}\tau=0.\tag{C 5}$$

We denote the intersections of periodic orbits and $\theta=0$ as $(0,\eta_1^C)$ and $(0,\eta_2^C)$, $(0<\eta_1^C<3/2\pi,\ \eta_2^C<0)$. Thus (C 5) gives, using (5.28),

$$\int_{\eta_1^C}^{\eta_2^C}F_1(\eta,C)\mathrm{d}\eta+\tilde{\mathscr{T}}\int_{\eta_1^C}^{\eta_2^C}F_2(\eta,C)\mathrm{d}\eta=0,\tag{C 6}$$

where

$$F_1=\frac{\eta\left(\pi(4\eta(375-274\pi\eta)+27C\pi(35-34\pi\eta))+36(35-34\pi\eta)\ln\left(\frac{3}{2\pi}-\eta\right)\right)}{2880(3-2\pi\eta)^2\sqrt{\pi(9C\pi+8\eta)+12\ln\left(\frac{3}{2\pi}-\eta\right)}},\tag{C 7a}$$

$$F_2=-\frac{8\pi^5\eta^2}{27(3-2\pi\eta)^2\sqrt{\pi(9C\pi+8\eta)+12\ln\left(\frac{3}{2\pi}-\eta\right)}}.\tag{C 7b}$$

As $C\to 4\ln(2\pi/3)/3\pi^2$ and $\eta_{1,2}^C\to 0$, we have

$$\eta_{1,2}^C\approx\pm\frac{3\sqrt{3\pi^2C+4\ln\frac{3}{2\pi}}}{2\sqrt{2}\pi},\tag{C 8}$$

$$F_1\approx\frac{11\pi\eta^2}{432\sqrt{3\left(3\pi^2C+4\ln\frac{3}{2\pi}\right)}},\quad F_2\approx-\frac{8\pi^5\eta^2}{243\sqrt{3\left(3\pi^2C+4\ln\frac{3}{2\pi}\right)}}.\tag{C 9}$$

Thus, the condition (C 6) for small-amplitude orbits approximately is $\tilde{\mathscr{T}}=99/128\pi^4(\approx 0.0079)$, consistent with (5.19*a*).

For large C, numerical evaluation of the integrals in (C 6) is difficult. In this case, the unperturbed closed orbit in figure 8 can be divided into two parts, which approximately are

$$\eta_{\mathrm{upper}}=\frac{3}{2\pi}-\exp\left[-\frac{3}{4}\pi^2\left(C-\theta^2\right)\right],\quad \eta_{\mathrm{lower}}=-\frac{9}{8}\pi\left(C-\theta^2\right).\tag{C 10a,b}$$

https://doi.org/10.1017/jfm.2014.136 Published online by Cambridge University Press

Thus (C 5) gives, using $\eta \mathrm{d}\tau = \mathrm{d}\theta$,

$$I_{\text{upper}} + I_{\text{lower}} = 0, \tag{C 11}$$

with

$$I_{\text{upper}} = \int_{\theta_1}^{\theta_2} \frac{20\eta_{\text{upper}}(-99 + 128\pi^4\tilde{\mathscr{T}} + 42\pi\eta_{\text{upper}}) + 81\pi(-35 + 34\pi\eta_{\text{upper}})\theta^2}{23040(-3 + 2\pi\eta_{\text{upper}})}\mathrm{d}\theta, \tag{C 12}$$

$$I_{\text{lower}} = \int_{\theta_2}^{\theta_1} \frac{20\eta_{\text{lower}}(-99 + 128\pi^4\tilde{\mathscr{T}} + 42\pi\eta_{\text{lower}}) + 81\pi(-35 + 34\pi\eta_{\text{lower}})\theta^2}{23040(-3 + 2\pi\eta_{\text{lower}})}\mathrm{d}\theta. \tag{C 13}$$

For the leading-order approximation, $\theta_{1,2} = \mp\sqrt{C}$, which gives

$$\begin{aligned} I_{\text{upper}} = {} & \frac{1}{11520\pi^{5/2}}\left(\sqrt{C\pi}(432 + 270\pi + 459C\pi^3 + 1280\pi^5\tilde{\mathscr{T}})\right. \\ & - 280\sqrt{3}\pi^{3/2}\mathrm{D}_+\left[\frac{1}{2}\sqrt{3C}\pi\right] \\ & \left. + 4\sqrt{3}\exp\left[\frac{3C\pi^2}{4}\right](9 - 160\pi^4\tilde{\mathscr{T}})\mathrm{erf}\left[\frac{1}{2}\sqrt{3C}\pi\right]\right), \end{aligned} \tag{C 14}$$

$$\begin{aligned} I_{\text{lower}} = {} & \frac{1}{4320\pi^2\sqrt{4 + 3C\pi^2}}\left(3\pi\sqrt{C\left(4 + 3C\pi^2\right)}\left(27 + 18C\pi^2 + 160\pi^4\tilde{\mathscr{T}}\right)\right. \\ & + 2\sqrt{3}\left(27 + 54C\pi^2 + 160\pi^4\tilde{\mathscr{T}}\right) \\ & \left.\times \ln\left[1 + \frac{1}{2}\pi\left(3C\pi - \sqrt{3}\sqrt{C\left(4 + 3C\pi^2\right)}\right)\right]\right), \end{aligned} \tag{C 15}$$

where $\mathrm{D}_+(x)$ is the Dawson integral $\exp[-x^2]\int_0^x \exp[t^2]\mathrm{d}t$ and $\mathrm{erf}(x)$ is the error function. For large C, the dominant part of (C 5) gives

$$\tilde{\mathscr{T}} = \frac{9}{160\pi^4}(\approx 0.000577) \tag{C 16}$$

(see figure 13).

As $\eta_{1,2}^C$ increases from zero, we can use (C 6) to numerically evaluate $\tilde{\mathscr{T}}$ for the existence of a limit cycle in the perturbed system (5.25), as seen in figure 13. Because $\tilde{T}$ falls as C increases, we infer that the Hopf bifurcation is supercritical. In figure 14, it is observed that limit cycles predicted from the Mel'nikov analysis agree well with the fourth-order amplitude equations (5.17) and the second-order asymptotics (5.25). Interestingly, the oscillation grows to large amplitude at finite $\tilde{\mathscr{T}}$, a prediction supported by solutions of the fourth-order system (5.17). When $\tilde{\mathscr{T}}$ falls sufficiently below $9/160\pi^4$, the limit cycle of (5.17) is destroyed and the solution diverges; this can be explained by assuming $\hat{T} + 405/8\pi^4 \sim O(\hat{\mathscr{L}}^{1/2})$, in which case the term $\tilde{\mathscr{T}}\theta_\tau$ in (5.25) is promoted to leading order, turning the limit cycles in figure 8 into divergent spirals. Our simulations indicate that there exists a

https://doi.org/10.1017/jfm.2014.136 Published online by Cambridge University Press

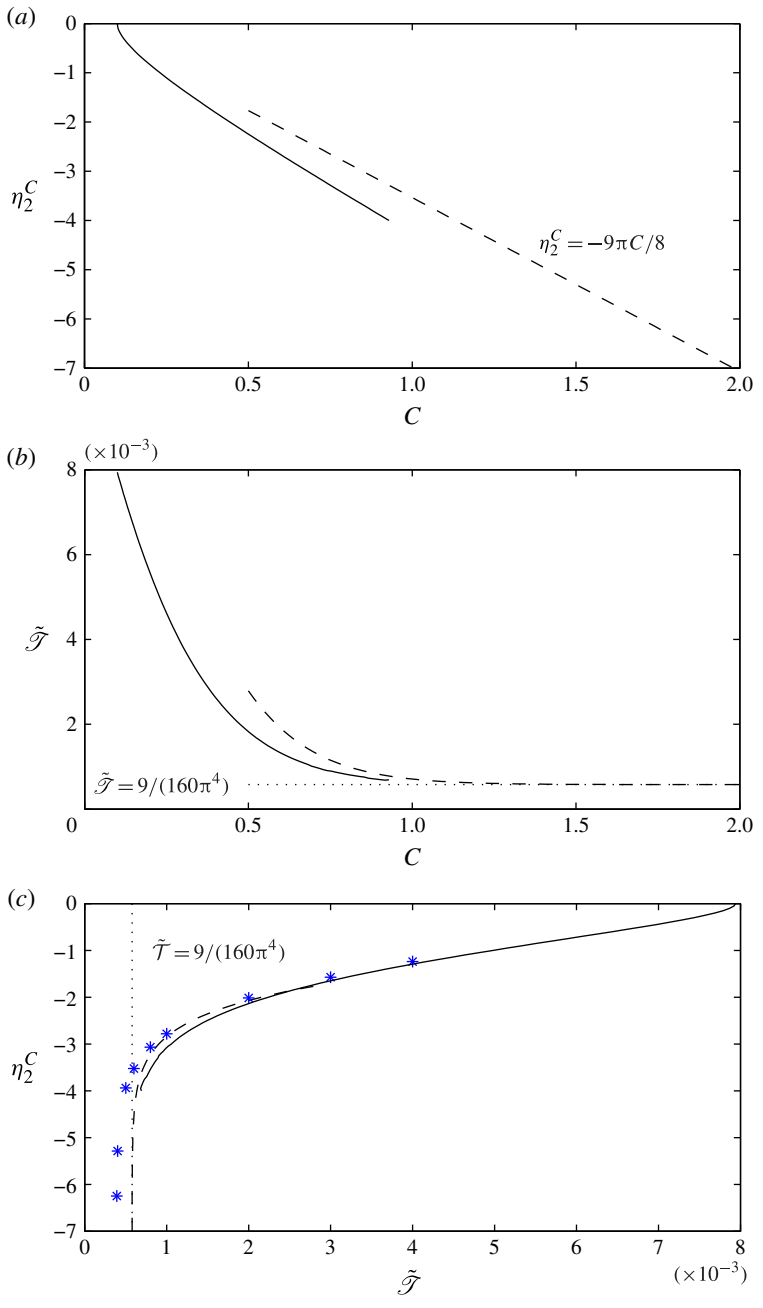


FIGURE 13. (Colour online) Relations between η_2^C, C and $\tilde{\mathscr{T}}$ in (C 6). The solid line is from (C 6) as η_2^C decreases from 0 to -4 and the dashed line is from (C 10) (*a*) and from (C 11) (*b*) as C increases from 0.5 to 2. The dotted line is the asymptote (C 16). Eliminating C, the relation between η_2^C and $\tilde{\mathscr{T}}$ is given in (*c*), in which the stars denote results from the fourth-order system (5.17) with $\hat{\mathscr{L}} = 0.4$.

https://doi.org/10.1017/jfm.2014.136 Published online by Cambridge University Press

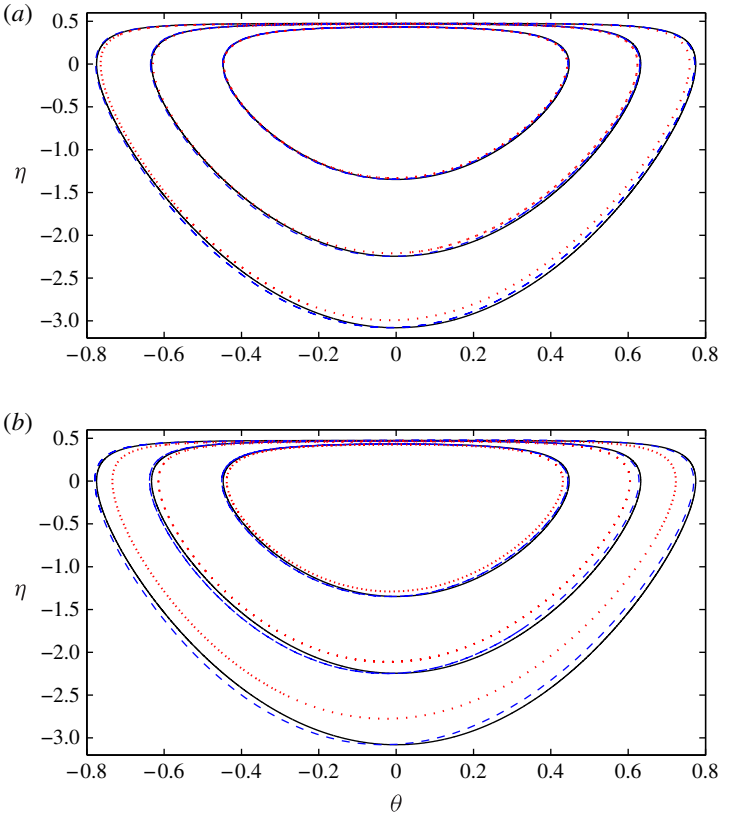


FIGURE 14. (Colour online) Contours from (5.28) (solid) and limit cycles from (5.25) (dashed) and (5.17) (dotted) with $C = 0.3$, 0.5 and 0.7 (increasing outwards) and corresponding respectively to $\tilde{\mathscr{T}} = 0.0038$, 0.0018 and 0.0010, where $\hat{\mathscr{L}} = 0.1$ (*a*) and 0.4 (*b*).

critical value of $\hat{\mathscr{L}}$ between 1 and 10, above which the limit cycle diverges after a period-doubling cascade but below which no period-doubling appears before the limit cycle diverges.

REFERENCES

BERTRAM, C. D. & BUTCHER, K. S. A. 1992 A collapsible-tube oscillator is not readily enslaved to an external resonator. *J. Fluids Struct.* **6** (2), 163–180.

BERTRAM, C. D. & TSCHERRY, J. 2006 The onset of flow-rate limitation and flow-induced oscillations in collapsible tubes. *J. Fluids Struct.* **22** (8), 1029–1045.

CAI, Z. X. & LUO, X. Y. 2003 A fluid–beam model for flow in a collapsible channel. *J. Fluids Struct.* **17**, 125–146.

CHAKRABORTY, D., PRAKASH, J. R., FRIEND, J. & YEO, L. 2012 Fluid-structure interaction in deformable microchannels. *Phys. Fluids* **24**, 102002.

GROTBERG, J. B. & JENSEN, O. E. 2004 Biofluid mechanics in flexible tubes. *Annu. Rev. Fluid Mech.* **36**, 121–147.

GUNERATNE, J. C. & PEDLEY, T. J. 2006 High-Reynolds-number steady flow in a collapsible channel. *J. Fluid Mech.* **569**, 151–184.

https://doi.org/10.1017/jfm.2014.136 Published online by Cambridge University Press

HEIL, M. & HAZEL, A. L. 2006 `oomph-lib` An object-oriented multi-physics finite-element library. In *Fluid-Structure Interaction* (ed. M. Schäfer & H.-J. Bungartz), pp. 19–49. Springer (`oomph-lib` is available as open-source software at http://www.oomph-lib.org).

HEIL, M. & HAZEL, A. L. 2011 Fluid–structure interaction in internal physiological flows. *Annu. Rev. Fluid Mech.* **43**, 141–162.

HOLMES, P. J. 1980 Averaging and chaotic motions in forced oscillations. *SIAM J. Appl. Maths* **38** (1), 65–80.

JENSEN, O. E. & HEIL, M. 2003 High-frequency self-excited oscillations in a collapsible-channel flow. *J. Fluid Mech.* **481**, 235–268.

KNOWLTON, F. P. & STARLING, E. H. 1912 The influence of variations in temperature and blood-pressure on the performance of the isolated mammalian heart. *J. Physiol.* **44** (3), 206–219.

KUDENATTI, R. B., BUJURKE, N. M. & PEDLEY, T. J. 2012 Stability of two-dimensional collapsible-channel flow at high-Reynolds-number. *J. Fluid Mech.* **705**, 371–386.

LIU, H. F., LUO, X. Y. & CAI, Z. X. 2012 Stability and energy budget of pressure-driven collapsible channel flows. *J. Fluid Mech.* **705**, 348–370.

LUO, X. Y. & PEDLEY, T. J. 1996 A numerical simulation of unsteady flow in a two-dimensional collapsible channel. *J. Fluid Mech.* **314**, 191–225.

LUO, X. Y. & PEDLEY, T. J. 1998 The effects of wall inertia on flow in a two-dimensional collapsible channel. *J. Fluid Mech.* **363**, 253–280.

LUO, X. Y. & PEDLEY, T. J. 2000 Multiple solutions and flow limitation in collapsible channel flows. *J. Fluid Mech.* **420**, 301–324.

MANDRE, S. & MAHADEVAN, L. 2010 A generalised theory of viscous and inviscid flutter. *Proc. R. Soc. Lond.* A **466**, 141–156.

PEDLEY, T. J. 1992 Longitudinal tension variation in collapsible channels - a new mechanism for the breakdown of steady flow. *Trans. ASME: J. Biomech. Engng* **114** (1), 60–67.

PIHLER-PUZOVIĆ, D. & PEDLEY, T. J. 2013 Stability of high-Reynolds-number flow in a collapsible channel. *J. Fluid Mech.* **714**, 536–561.

STEWART, P. S., HEIL, M., WATERS, S. L. & JENSEN, O. E. 2010 Sloshing and slamming oscillations in a collapsible channel flow. *J. Fluid Mech.* **662**, 288–319.

STEWART, P. S., WATERS, S. L. & JENSEN, O. E. 2009 Local and global instabilities of flow in a flexible-walled channel. *Eur. J. Mech. (*B*/Fluids)* **28** (4), 541–557.

WANG, J. W., CHEW, Y. T. & LOW, H. T. 2009 Effects of downstream system on self-excited oscillations in collapsible tubes. *Commun. Numer. Meth. Engng* **25** (5), 429–445.

WHITTAKER, R. J., HEIL, M., BOYLE, J., JENSEN, O. E. & WATERS, S. L. 2010*a* The energetics of flow through a rapidly oscillating tube. Part 2. Application to an elliptical tube. *J. Fluid Mech.* **648**, 123–153.

WHITTAKER, R. J., HEIL, M., JENSEN, O. E. & WATERS, S. L. 2010*b* Predicting the onset of high-frequency self-excited oscillations in elastic-walled tubes. *Proc. R. Soc. Lond.*A **466**, 3635–3657.

WHITTAKER, R. J., WATERS, S. L., JENSEN, O. E., BOYLE, J. & HEIL, M. 2010*c* The energetics of flow through a rapidly oscillating tube. Part 1. General theory. *J. Fluid Mech.* **648**, 83–121.

XU, F., BILLINGHAM, J. & JENSEN, O. E. 2013 Divergence-driven oscillations in a flexible-channel flow with fixed upstream flux. *J. Fluid Mech.* **723**, 706–733.

https://doi.org/10.1017/jfm.2014.136 Published online by Cambridge University Press